CORONAVIRUS

Cardiac tissue model of immune-induced dysfunction reveals the role of free mitochondrial DNA and the therapeutic effects of exosomes

Rick Xing Ze Lu[1,2], Naimeh Rafatian[1], Yimu Zhao[1,3], Karl T. Wagner[1], Erika L. Beroncal[2,4], Bo Li[5], Carol Lee[5], Jingan Chen[1], Eryn Churcher[6], Daniel Vosoughi[7,8], Chuan Liu[1], Ying Wang[1,3], Andrew Baker[6], Uriel Trahtemberg[6,9], Bowen Li[1,10], Agostino Pierro[5,11], Ana C. Andreazza[2,4,12], Claudia C. dos Santos[6], Milica Radisic[1,2,3,13,14]*

Despite tremendous progress in the development of mature heart-on-a-chip models, human cell–based models of myocardial inflammation are lacking. Here, we bioengineered a vascularized heart-on-a-chip with circulating immune cells to model severe acute respiratory syndrome coronavirus 2 (SARS-CoV-2)–induced acute myocarditis. We observed hallmarks of coronavirus disease (COVID-19)–induced myocardial inflammation, as the presence of immune cells augmented the secretion of proinflammatory cytokines, triggered progressive impairment of contractile function, and altered intracellular calcium transients. An elevation of circulating cell-free mitochondrial DNA (ccf-mtDNA) was measured first in the heart-on-a-chip and then validated in COVID-19 patients with low left ventricular ejection fraction, demonstrating that mitochondrial damage is an important pathophysiological hallmark of inflammation-induced cardiac dysfunction. Leveraging this platform in the context of SARS-CoV-2–induced myocardial inflammation, we established that administration of endothelial cell–derived exosomes effectively rescued the contractile deficit, normalized calcium handling, elevated the contraction force, and reduced the ccf-mtDNA and cytokine release via Toll-like receptor–nuclear factor κB signaling axis.

INTRODUCTION

Whereas numerous studies report bioengineering models of fibrosis and cardiomyopathies (1–3), inflammatory conditions of the heart such as myocarditis are largely understudied. Most of the current mechanistic understanding of myocarditis comes from experiments in differentially susceptible rodent strains, which inevitably raises questions regarding the applicability of rodent-derived cardiac functional and immune system responses to human cardiovascular physiology. The absence of definitive therapeutic interventions for inflammatory heart conditions, such as myocarditis, is exacerbated by the lack of reliable biomarkers, difficulties in reaching a confirmatory diagnosis, and paucity of predictive human models for therapeutic testing. These factors collectively underscore the imperative nature of our work here. The successful modeling of heart inflammation hinges on the amalgamation of key advancements including (i) high-fidelity induced pluripotent stem cell (iPSC)–derived functional cardiac tissues, (ii) establishment of a perfusable vasculature,

(iii) inclusion of immune cells, and (iv) the ability to gather functional readouts such as contractility, calcium handling, and electrical excitability in a single system.

While the clinical occurrence of acute myocarditis following severe acute respiratory syndrome coronavirus 2 (SARS-CoV-2) infection is well documented, the underlying biological mechanisms remain elusive. It was initially hypothesized that the internalization of viral RNA into the cardiomyocytes directly via the angiotensin-converting enzyme 2 (ACE2) (4, 5) causes heart damage by impairing electromechanical functions (6–8). As the COVID-19 pandemic progressed, it became increasingly appreciated that systemic inflammation secondary to SARS-CoV-2 infection leads to cardiac complications, further motivating the development of human cell–based vascularized disease models.

Complex conditions, such as viral-induced myocardial inflammation, require new therapeutics. We focused on extracellular vesicles (EVs) as these subcellular entities, with an average diameter ranging between 80 and 200 nm, are pivotal mediators of intercellular communication. They achieve this by encapsulating and transferring selective biomolecules—microRNA (miRNA), mRNA, proteins, and metabolites—from their parent cell to recipient cells, all without necessitating direct cell-to-cell contact (9). In addition, EVs are intrinsically biocompatible, biodegradable, and exhibit minimal cytotoxicity. Furthermore, EVs derived from human umbilical endothelial cells (HUVECs) have previously demonstrated promising regenerative, anti-inflammatory, and cardioprotective properties in preclinical settings (10–12), hence their selection for inflammation management in our model.

Here, we used an organ-on-a-chip system, termed integrated vasculature for assessing dynamic events (InVADE), which integrates iPSC-derived cardiomyocytes, an endothelialized microvessel structure termed Angiotube and peripheral blood mononuclear cells (PBMCs) to capture the complex cascade of events driving immune

[1]Institute of Biomedical Engineering, University of Toronto, Toronto, ON M5S 3G9, Canada. [2]Mitochondrial Innovation Initiative, MITO2i, University of Toronto, Toronto, ON M5S 1A8, Canada. [3]Toronto General Hospital Research Institute, University Health Network, Toronto, ON M5G 2C4, Canada. [4]Department of Pharmacology and Toxicology, University of Toronto, Toronto, ON M5S 1A8, Canada. [5]Hospital for Sick Children, Toronto, ON M5G 1X8, Canada. [6]Interdepartmental Division of Critical Care, Keenan Research Centre for Biomedical Science, St. Michael's Hospital, Unity Health Toronto, Toronto, ON M5B 1W8, Canada. [7]Latner Thoracic Laboratories, Toronto General Hospital Research Institute, University Health Network, Toronto, ON M5G 2C4, Canada. [8]Institute of Medical Science, University of Toronto, Toronto, ON M5S 1A8, Canada. [9]Galilee Medical Center, Nahariya, Israel. [10]Leslie Dan Faculty of Pharmacy, University of Toronto, Toronto, ON M5S 3M2, Canada. [11]Department of Surgery, University of Toronto, Toronto, ON M5T 1P5, Canada. [12]Department of Psychiatry, University of Toronto, Toronto, ON M5S 1A8, Canada. [13]Department of Chemical Engineering and Applied Chemistry, University of Toronto, Toronto, ON M5S 3D5, Canada. [14]Terrence Donnelly Centre for Cellular & Biomolecular Research, University of Toronto, Toronto, ON, M5S 3E1.
*Corresponding author. Email: m.radisic@utoronto.ca

cell–induced cardiac dysfunction. We used SARS-CoV-2 as an example viral challenge, inducing acute myocarditis phenotype within our vascularized heart-on-a-chip. This necessitated the modification of our platform design to mitigate potential hazards and ensure compatibility with containment level 3 (CL-3) facility working conditions. Briefly, upon SARS-CoV-2 application, PBMCs infiltrated the cardiac tissue from the vascular compartment, creating a hyperinflammatory microenvironment that resulted in electromechanical dysfunction of the cardiac tissue. Impairment of myocardial mitochondria, along with the release of cell-free mitochondrial DNA (mtDNA) was found to be a crucial pathophysiological hallmark of the developing myocarditis phenotype. Notably, plasma samples from intensive care unit patients with COVID-19 exhibit elevated levels of circulating cell-free mtDNA, correlating with systemic inflammation and inversely associated with cardiac function. HUVEC-EVs imparted a cardiovascular-protective effect and carried immunomodulatory miRNAs that alleviated SARS-CoV-2–induced myocardial injury through Toll-like receptor–nuclear factor κB (TLR–NF-κB) axis, which subsequently mitigated the proinflammatory response and mitochondrial impairment. These findings suggest that HUVEC-EVs may serve as a promising immunomodulatory agent for the transfer of anti-inflammatory miRNAs to maintain heart homeostasis and prevent inflammatory injury.

RESULTS

Immune cell extravasation and inflammatory cytokine secretion arise upon SARS-CoV-2 application to vascularized cardiac tissue

The InVADE system (Fig. 1) was leveraged to capture aspects of immune cell–activated cardiac tissue dysfunction in the presence of human-derived PBMCs. HUVECs were grown inside a hollow biocompatible polymeric vessel (100 μm wide by 100 μm height) and then cultured with a human iPSC-derived cardiac construct (Fig. 1A) to generate perfusable functional vascularized heart tissues. Immune cells, PBMCs were perfused through the endothelialized internal lumen of the microfluidic scaffold via a gravity-driven flow to investigate how SARS-CoV-2 presence and immune cells interact to aggravate heart function, as well as to screen for the therapeutic benefit of EVs (Fig. 1B). The fluid shear stress exerted within the bioscaffold was estimated to be approximately 1.3 dyne cm^{-2}, which closely aligns with the physiological flow conditions experienced by endothelial cells within post-capillary venules (13), where immune cell infiltration is mostly observed in patients with COVID-19 (14–18). To validate the utility of the InVADE model, SARS-CoV-2 was first introduced into a vascular channel to mimic in vivo infection at a multiplicity of infection (MOI) of 0.1, which is considered physiologically relevant (19). Following 1.5 hours of viral infection, fluorescently labeled PBMCs were perfused into each sample (Fig. 1C) and samples were subjected to hydrostatic pressure-driven flow. After 72 hours of immune cell introduction, 1,1′-dioctadecyl-3,3,3′,3′-tetramethylindocarbocyanine perchlorate (DiI)–stained PBMCs (Fig. 2A and fig. S1A), including CD3^{+} T lymphocytes (fig. S1B), were observed to extravasate from the vascular compartment into the cardiac tissue through the 15 μm by 15 μm microholes of the microfluidic scaffold. The local accumulation of immune cells was mirrored by increased production of cytokines and chemokines, including interleukin-6 (IL-6), IL8, and monocyte chemoattractant protein-1 (MCP-1) (Fig. 2B and fig. S2A), which further help to attract immune cells toward the site of inflammation guided by chemotactic signals. Monolayer transwell experiments confirmed similar levels of viral propagation in both cardiomyocyte (CM) alone and the cocultures of CM and PBMC, approximately 2000-fold lower than those of Vero E6 cells, as expected (fig. S3).

The presence of immune cells leads to a progressive cardiac tissue dysfunction upon SARS-CoV-2 infection

Cantilevers incorporated into the InVADE platform allow for noninvasive monitoring of contractile force using cantilever displacement (fig. S4A), via previously generated calibration curves (fig. S4B). Although SARS-CoV-2 presence alone did not induce a contractile deficit in the cardiac tissue (Fig. 2, C and D, and fig. S4C), the introduction of PBMCs after SARS-CoV-2 inoculation led to a notable contractile deficit at 72 hours after infection (Fig. 2, C and D). This was in accord with the findings that highlight the role of infiltrating PBMCs in generating an inflammatory microenvironment in the SARS-CoV-2–infected cardiac tissues that ultimately culminated in disruption of the contractile proteins, such as troponin T, within the cardiac tissue (Fig. 2A). The electrical excitability of the cardiac tissue treated with PBMCs progressively declined with increasing viral infection durations, as evidenced by the rise in the excitation threshold (ET), which denotes the minimal voltage required to generate synchronous contraction (Fig. 2E). Moreover, SARS-CoV-2 inoculation with PBMCs seemingly disrupted intracellular calcium homeostasis (Fig. 2F), as suggested by the significant reduction in the intracellular calcium transient amplitude (Fig. 2G) and calcium influx kinetics (Fig. 2H) as compared to the control group, while the intracellular calcium efflux and decay time constant remained unchanged (fig. S2B). We highlight that the integration of PBMCs in the absence of SARS-CoV-2 does not impinge upon the function of cardiac tissues (fig. S4, C and E). This denotes that cooperative interactions of SARS-CoV-2 with immune cells potentially exacerbate the electrochemical regulation of the cardiac tissues. These findings are consistent with our previous study which examined in great detail the introduction of PMBCs alone without SARS-CoV-2 into the endothelialized InVADE platform, documenting no elevation in cytokine secretion or significant immune cell extravasation (20).

Given that cardiac mitochondria are critical in upholding cardiac homeostasis through their role in providing the energy needed for cardiac excitation-contraction coupling and regulating essential intracellular pathways related to cellular survival, the effect of increased inflammation on mitochondrial function was assessed. Transmission electron microscopy (TEM) imaging identified significant mitochondria impairment demonstrated by mitochondrial loss and increased vacuolization in SARS-CoV-2/PBMC–exposed cardiac tissues (Fig. 2I). This was also accompanied by elevated levels of ccf-mtDNA. Specifically, ccf-ND1 and ccf-ND4 were observed in the culture medium, indicating the release of the free mtDNA from the cardiac tissue (Fig. 2J).

Ccf-mtDNA is a key predictor of cardiac dysfunction in patients with COVID-19

To determine whether an increase in plasma ccf-mtDNA concentration is reflected in COVID-19 patients with cardiovascular complications, assessments were performed in 40 patients admitted to the medical-surgical intensive care units at St. Michael's Hospital with acute respiratory failure and suspicion of COVID-19 in Toronto, Canada, between March 2020 and March 2022. The median patient age was 61.6 years [interquartile range (IQR): 51.3 to 71.0], ranging from
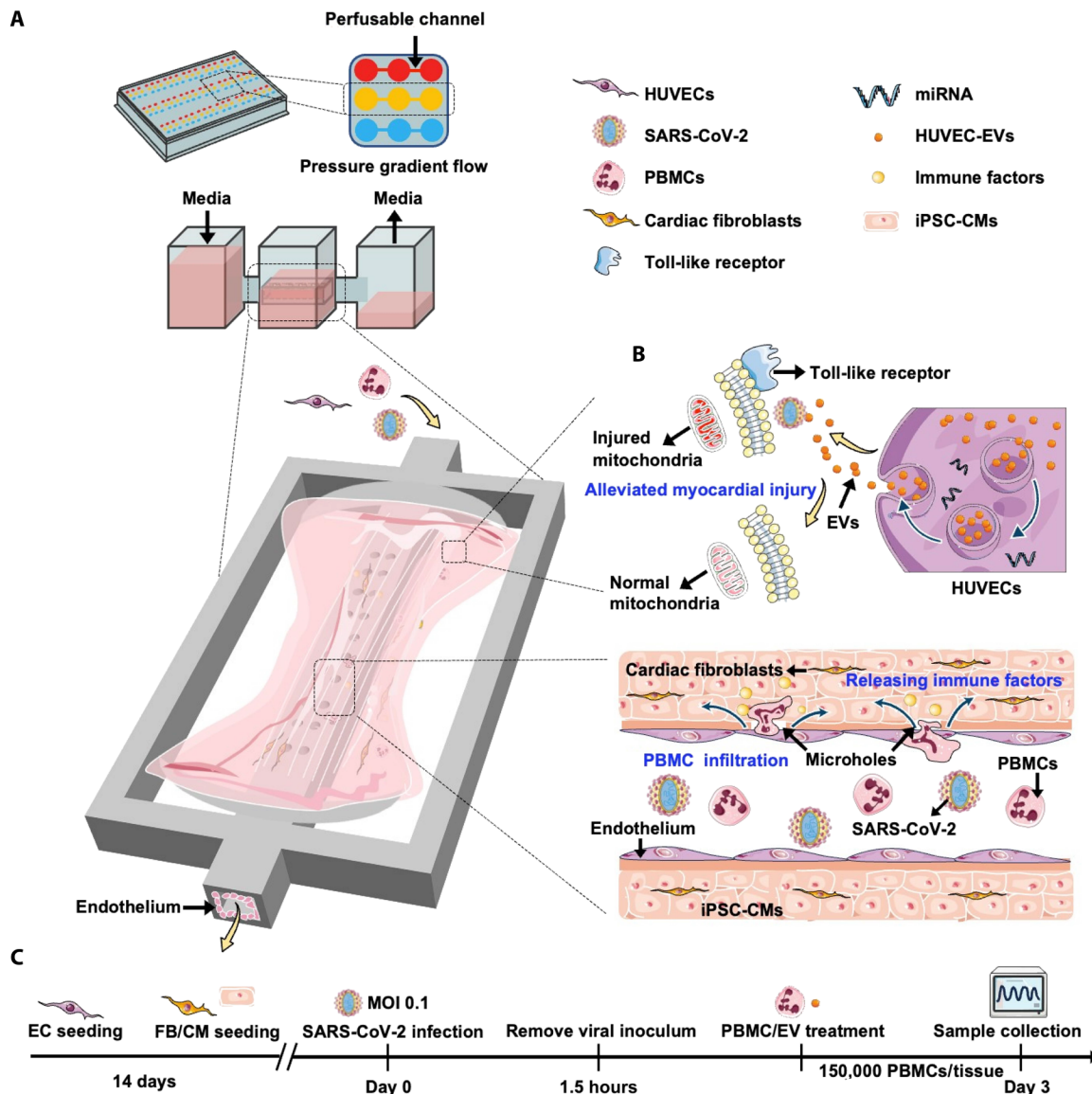
Fig. 1. Vascularized heart-on-a-chip model for SARS-CoV-2–induced myocardial inflammation. (**A**) Illustration of the components of the InVADE system. Endothelial cells were grown within the luminal space, and iPSC-derived cardiac tissues were cultured within the parenchymal space. Perfusion is initiated through a hydrostatic pressure gradient within the vascular compartment. (**B**) Schematic of the perfusion of human PBMCs through the vasculature. PBMCs can infiltrate into the cardiac tissue compartment through 15-μm microholes. EVs were added to mitigate mitochondrial dysfunction. (**C**) Experimental timeline showing the sequence of SARS-CoV-2 infection and PBMC addition.

31 to 90 years (Table 1). Half of the admitted patients were confirmed to be SARS-CoV-2–positive by polymerase chain reaction (PCR) tests. Patients with COVID-19 ($n = 20$) had 2.49-fold higher ccf-mtND1 (median 11,102 copies/ml [IQR: 5988 to 27,885]) and 2.40-fold higher ccf-mtND4 (median 8849 copies/ml [IQR: 5408–20,614]) levels compared to SARS-CoV-2–negative patients ($n = 20$) (ccf-mtND1 median 4463 copies/ml [IQR: 1392 to 12,385], $P = 0.0316$; ccf-mtND4 median 3964 copies/ml [IQR: 1049 to 7692], $P = 0.00246$) (Table 1). Of note, 1.62-fold higher ccf-mtND1 and 2.11-fold higher ccf-mtND4 were detected in COVID-19 patients with left ventricular ejection fraction (LVEF) < 50% compared to COVID-19 patients with LVEF > 50% (Fig. 3A). Mortality rates higher by 3.5-fold were documented for the former compared to the latter group of patients (70% versus 20%;

Fig. 3A). Within the COVID-19 patient cohort, a significant negative association was found between plasma ccf-mtDNA levels with LVEF (Fig. 3B), suggesting that elevated concentration of ccf-mtDNA is closely linked to increased risk of cardiac dysfunction. Furthermore, a direct linear correlation between ccf-mtDNA levels and systemic inflammation was observed (Fig. 3B), consistent with clinical observations in patients experiencing COVID-19 cardiac injury (21). Together, these results establish that a heart-on-a-chip system with circulating immune cells is capable of pinpointing potential biomarkers that closely align with clinical observations. Notably, the plasma concentration of ccf-mtDNA emerges as a robust marker indicative of both cardiac dysfunction and systemic inflammation and may facilitate early identification of patients with poor prognoses.
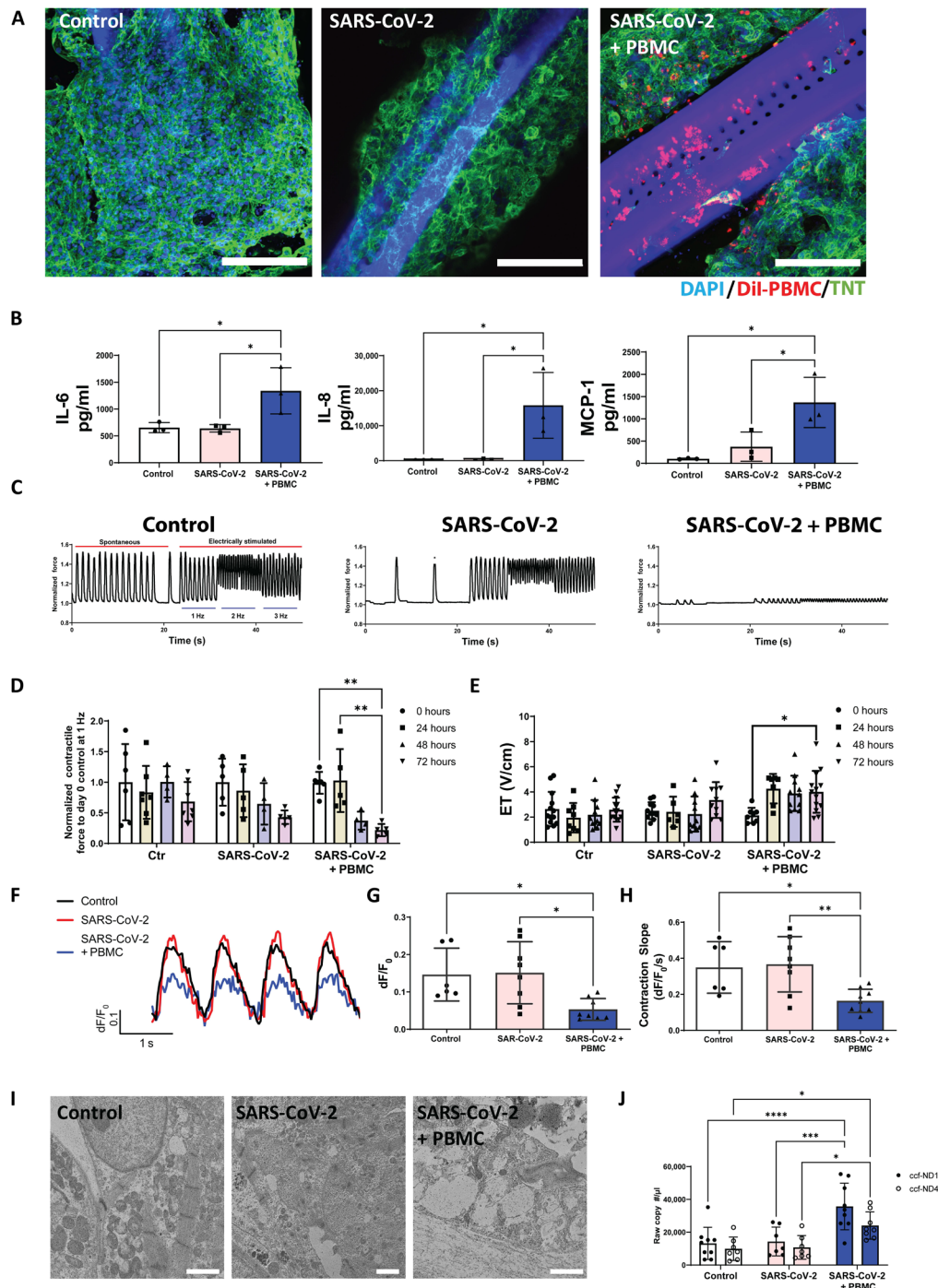
Fig. 2. The presence of PBMCs in SARS-CoV-2–infected heart-on-a-chip leads to progressive decline of cardiac tissues. (**A**) Representative confocal fluorescence microscopy images of local cardiac troponin T disruption in the presence of SARS-CoV-2 and PBMCs. DiI-labeled PBMC (red), nuclei labeled by 4′,6-diamidino-2-phenylindole (DAPI) (blue), and troponin T (green). Scale bars, 200 μm. (**B**) Analysis of proinflammatory cytokines and chemokines 72 hours after SARS-CoV-2 infection at MOI of 0.1. Data are means ± SD, $n = 3$. One-way analysis of variance (ANOVA) with Bartlett's test; $*P < 0.05$. (**C**) Representative normalized force of the cardiac tissue paced with increasing stimulation frequency 72 hours after SARS-CoV-2 infection at MOI of 0.1. (**D**) Excitation threshold and (**E**) normalized contraction force amplitude were measured under electrical stimulation at 0, 24, 48, and 72 hours after SARS-CoV-2 infection at MOI of 0.1. $N = 3$. Two-way ANOVA with Bartlett's test; $*P < 0.05$ and $**P < 0.01$. (**F**) Representative intracellular calcium transient of cardiac tissue 72 hours after infection with SARS-CoV-2 stimulated at 1 Hz. Quantification of the intracellular calcium transient properties after 72 hours of exposure to SARS-CoV-2: (**G**) calcium amplitude and (**H**) contraction slope. Data are means ± SD, $N = 3$. One-way ANOVA with Bartlett's test; $*P < 0.05$ and $**P < 0.01$. (**I**) Representative TEM images of cardiac tissue sections after infection with SARS-COV-2. Scale bars, 2 μm. (**J**) Circulating cell-free mitochondrial transcripts (ccf-mtND1 and ccf-mtND4) in cell culture medium. Data are means ± SD, $N = 3$. One-way ANOVA with Bartlett's test; $*P < 0.05$, $**P < 0.01$, $***P < 0.001$, and $****P < 0.0001$.

Table 1. Summary of the clinical characteristics and age of ICU-admitted patients.

	Clinical characteristics		
	COVID-19$^+$ ($n = 20$)	COVID-19$^-$ ($n = 20$)	
Demographics			*P* value
Age, median (IQR) (year)	62.5 (49.25–72.25)	67.0 (51.25–70.0)	
Distribution no. (%)			
18–40 years	2 (10)	2 (10)	
41–64 years	9 (45.0)	6 (30)	
≥65 years	9 (45.0)	12 (60)	
Clinical findings			
Lactate (IQR) (mM)	1.40 (1.10–1.80), 13/20	1.70 (1.20–2.30), 11/20	0.3146
pO2 (IQR) (mmHg)	77 (49.75–88.75), 16/20	85 (65.0–120.5), 17/20	0.0868
pH (IQR)	7.375 (7.310–7.435), 16/20	7.37 (7.315–7.415), 17/20	0.9187
Laboratory findings			
Total ccf-mtDNA ND1 (IQR) (count/µl)	11,102 (5,988–27,885)	4,463 (1,392–12,385)	0.0316
All patients			
Patients with LVEF < 50	17,319 (4,920–43,644)	2,879 (742–6,329)	0.0782
Patients with LVEF ≥ 50	10,650 (7,107–19,635)	7,238 (2,369–15,832)	0.7328
Total ccf-mtDNA ND4 (IQR) (count/µl)	8,849 (5,408–20,614)	3,964 (1,049–7,694)	0.00246
All patients			
Patients with LVEF < 50	13,737 (3,968–23,424)	2,136 (559–5,630)	0.0656
Patients with LVEF ≥ 50	6,516 (5,046–11,052)	4,565 (1,696–14,398)	0.7255

HUVEC-derived EVs are a potential therapy for SARS-CoV-2–induced contractile dysfunction and ccf-mtDNA release

As the inflammatory cascade starts off with endothelial cell and immune cell activation, we hypothesized that EVs derived from quiescent endothelial cells may be crucial in balancing the inflammatory response, given their notable contribution to the preservation of vascular homeostasis. EVs were isolated from quiescent HUVECs using precipitation method, and they displayed a cup-shaped morphology with an average diameter of 150 nm (Fig. 4A). Nanoparticle tracking analysis (NTA) revealed that EVs had a particle size of 155 nm, which was comparable in size to the TEM image (Fig. 4B). Western blot analysis confirmed the presence of exosomal markers, including CD9, CD63, and flotillin-1. In parallel, no intracellular protein calnexin was detected, indicating pure EV isolation (Fig. 4C).

When co-administered with PBMCs in the vascular compartment, EVs led to a decrease in the infiltration of PBMCs into the cardiac tissue (Fig. 4D). This was accompanied by a reduction in the measured proinflammatory cytokine responses, namely, IL-1α, IL-6, IL-8, and MCP-1 (Fig. 4E), and a notable shift toward anti-inflammatory phenotype, characterized by increased IL-10 levels (fig. S5A). A significant improvement in the contractile function of the SARS-CoV-2–infected heart-on-a-chip was observed (Fig. 4, F and G), leading to the restoration of electrical excitability properties to the levels comparable to those of control tissues (Fig. 4H). Furthermore, the amplitude (Fig. 4, I and J) and kinetics of intracellular calcium transient (Fig. 4K and fig. S5, B and E) were restored to normal levels, as were the sarcomere structure and mitochondrial ultrastructure (Fig. 4L). In addition, a decrease in ccf-mtDNA release into the extracellular environment was measured (Fig. 4M). Collectively, these results support the notion that

HUVEC-EVs can serve as a promising therapy for the restoration of mitochondrial integrity and repairing myocardial damage in the context of SARS-CoV-2 inflammation.

Extracellular vesicles contain miRNAs that suppress cellular proinflammatory responses

A miRNA sequencing (miRNA-seq) analysis of EV cargo was performed in search of miRNAs that regulate gene expression (data file S1). A total of 561 unique miRNAs were detected in isolated EVs (Fig. 5A) and ranked according to a fraction of total mapped miRNA reads. The top nine abundant miRNA in EVs were let-7b-5p, miR-1246, miR-126-3p, let-7a-5p, let-7c-5p, let-7i-5p, let-7f-5p, miR-16-5p, miR-125b-5p, and let-7e-5p (Fig. 5B). Subsequently, a Gene Ontology (GO) enrichment analysis was run to identify the biological processes that were significantly up-regulated in the dataset. The targeted pathways of the top nine most abundant miRNAs primarily clustered to biological processes relating to the TLR signaling pathway, immune response-regulating signaling pathway, and mitogen-activated protein kinase cascade (Fig. 5C). A Kyoto Encyclopedia of Genes and Genomes (KEGG) analysis found EV target signaling pathways associated with the TLR and tumor necrosis factor (TNF) signaling pathways (Fig. 5, D and E). As miRNAs typically repress mRNA function, this finding suggests that HUVEC-EVs contain miRNAs that help improve heart function by repressing TLR activation and subsequent inflammation induced by SARS-CoV-2 infection in endothelial cells, immune cells, and cardiomyocytes.

To validate these findings, TNF signaling was assessed following EV treatment of TNF-α–stimulated endothelial cells (Fig. 6A). After 2 hours of transfection, EVs were detected within HUVECs (Fig. 6B) along with an approximately sixfold increase in *TNFα*, a threefold
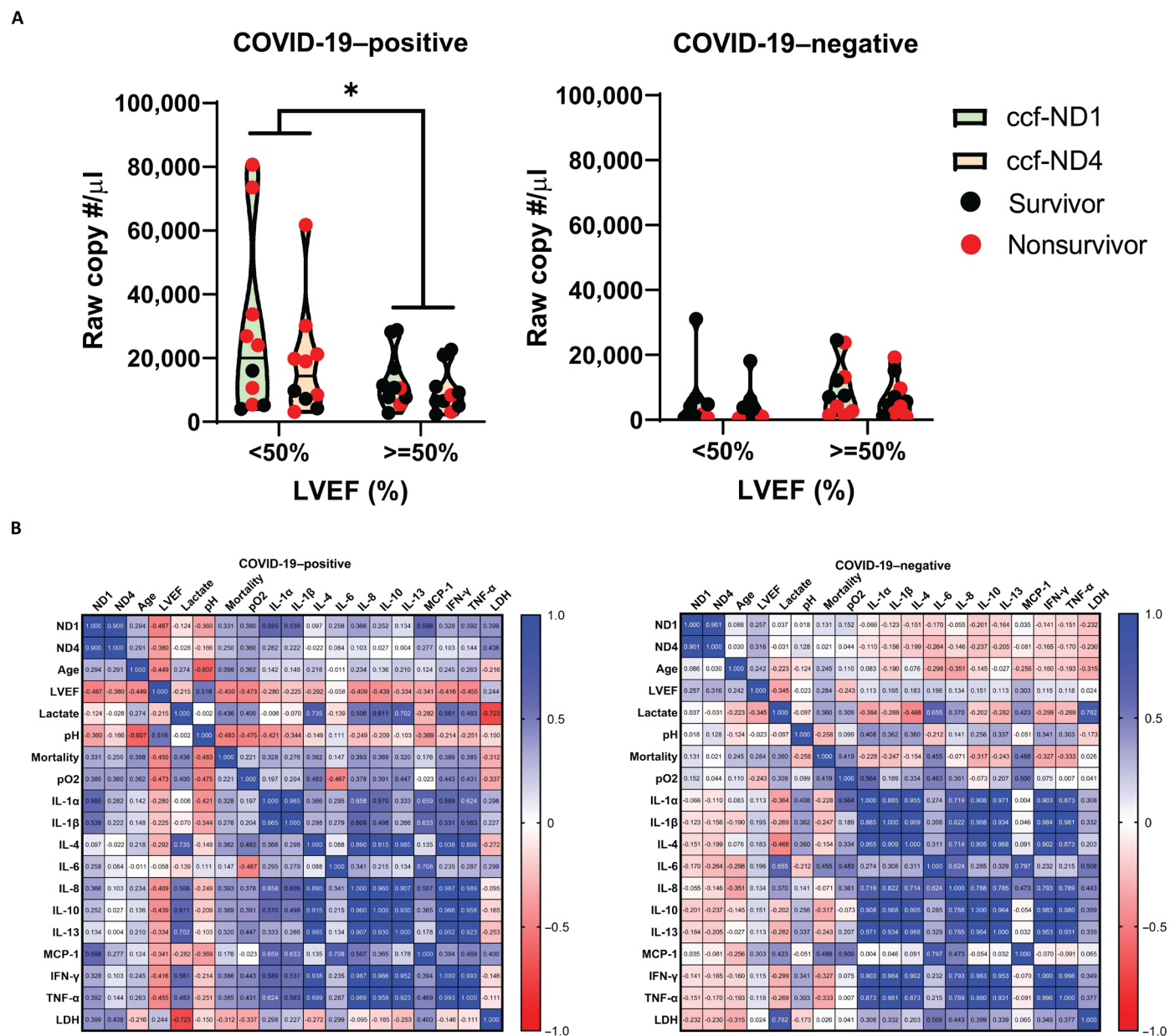
Fig. 3. Circulating cell-free mitochondrial DNA (ccf-mtDNA) is elevated in COVID-19 patients with contractile dysfunction. (**A**) Concentration of ccf-mtDNA in patient plasma samples. Data are means ± SD, $n = 20$. Two-way ANOVA with Holm-Sidak post hoc test; $*P < 0.05$. (**B**) Pearson's correlation of patient characteristics and plasma concentration of ccf-mtDNA within the COVID-19–positive and COVID-19–negative subgroups.

increase in *IL8* mRNA and suppression of proinflammatory genes (Fig. 6C). These results provide compelling evidence that EVs can mitigate inflammatory responses, as predicted by the GO and KEGG analyses.

## Extracellular vesicles target the TLR–NF-κB axis to mitigate proinflammatory responses

To characterize the effect of HUVEC-EVs on SARS-CoV-2–mediated proinflammatory response, PBMCs were treated with EVs and then stimulated with SARS-CoV-2. Uptake of EVs by PBMCs, confirmed by DiI-labeling of the EVs (Fig. 6D), resulted in the suppression of IL-8 activation (Fig. 6E and fig. S6), providing further evidence that

HUVEC-derived exosomes can blunt recruitment of immune cells to the site of inflammation (Fig. 6E). In addition, levels of extracellular reactive oxygen species (ROS) were 59% lowered following EV treatment, suggesting that EVs can protect mitochondrial components from damage and preserve their function (Fig. 6F).

We then used THP-1 dual-reporter cells, a validated monocyte cell model, to examine whether EVs can regulate NF-κB, a central regulator of innate immunity. THP-1 dual-reporter cells secrete inducible reporter proteins Lucia and secreted embryonic alkaline phosphate (SEAP), which reflect the activation of interferon-related factors (IRF) and NF-κB, respectively (Fig. 6G). THP-1 cells stimulated with SARS-CoV-2 secreted significantly more SEAP than
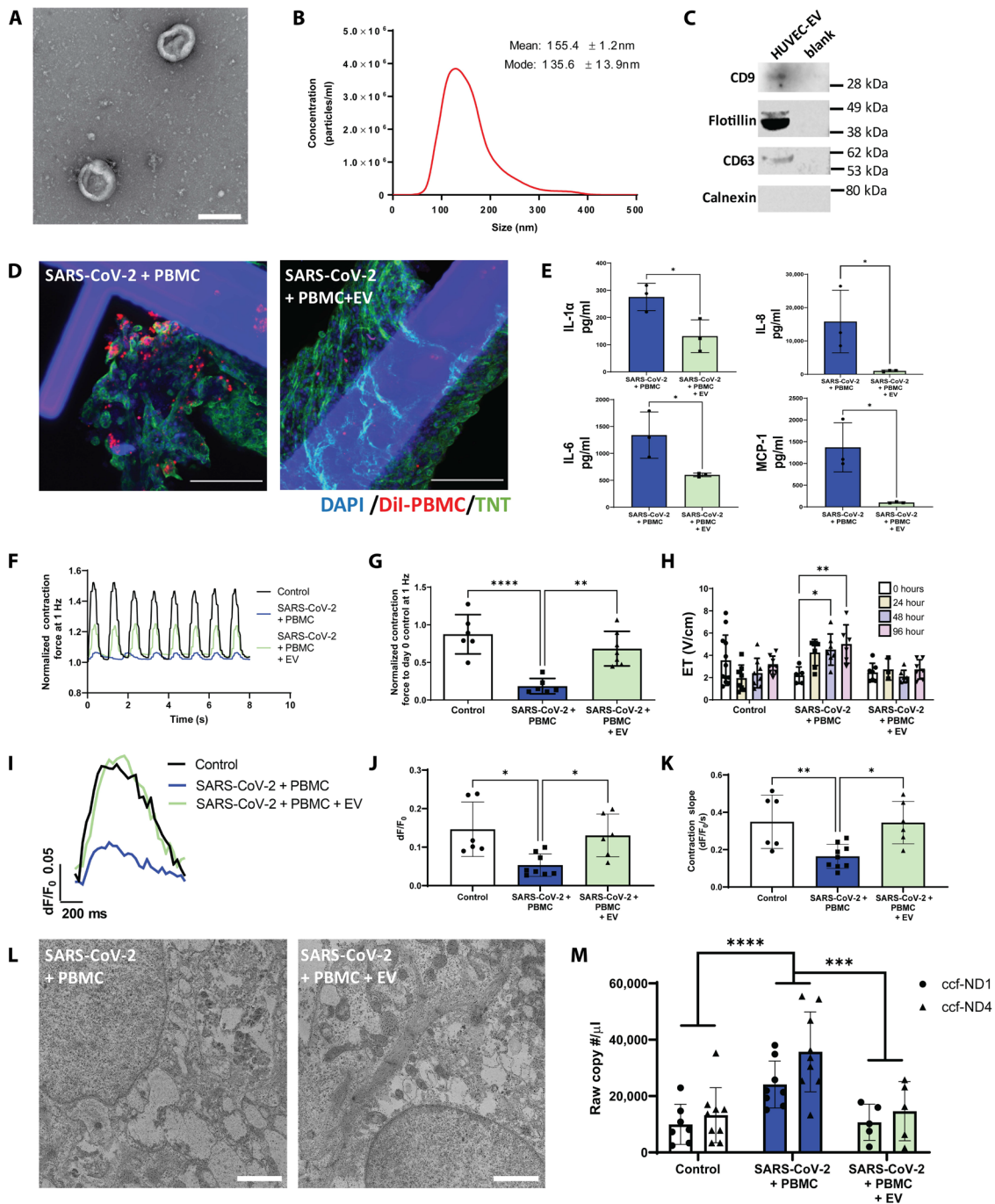
Fig. 4. HUVEC-EVs promote recovery of cardiac tissue functions following SARS-CoV-2 application in the presence of immune cells. (**A**) Representative TEM image of HUVEC-EVs. Scale bar, 200 nm. (**B**) Representative size distribution of HUVEC-EVs as measured by nanoparticle tracking analysis. (**C**) Immunoblots of HUVEC-EVs for the exosomal markers CD9, CD63, and Flot-1. The absence of calnexin demonstrates pure EV isolation. (**D**) Representative confocal fluorescence microscopy images of PBMCs infiltrating the human iPSC-derived cardiac tissue upon HUVEC-EV treatment. Dil-labeled PBMCs (red) and nuclei-labeled DAPI (blue). Scale bars, 100 μm. (**E**) Analysis of proinflammatory cytokines and chemokines from cardiac tissue 72 hours after SARS-CoV-2 infection at MOI of 0.1. Data are means ± SD, $n = 3$. Student's t test with Bartlett's test; *$P < 0.05$ and **$P < 0.01$. (**F**) Contractility traces at 1 Hz pacing. (**G**) Normalized contraction amplitude and (**H**) excitation threshold were measured under electrical stimulation at 1 Hz, 72 hours after SARS-CoV-2 infection at MOI of 0.1. (**I**) Representative intracellular calcium transient of cardiac tissue 72 hours after SARS-CoV-2 infection at 1 Hz. Quantification of the intracellular transient properties 72 hours after SARS-CoV-2 exposure and treatment with HUVEC-EVs: (**J**) amplitude and (**K**) contraction slope. Data are means ± SD, $N = 3$. Two-way ANOVA with Bartlett's test; *$P < 0.05$, **$P < 0.01$, ***$P < 0.001$, and ****$P < 0.0001$. (**L**) Representative TEM images of cardiac tissue after SARS-CoV-2 infection. Scale bars, 2 μm. (**M**) Concentration of ccf-mtDNA in cell culture medium collected 72 hours after SARS-CoV-2 exposure and treatment with HUVEC-EVs. Data are means ± SD, $N = 3$ from each experiment. Two-way ANOVA with Bartlett's test; *$P < 0.05$, **$P < 0.01$, ***$P < 0.001$, and ****$P < 0.0001$.
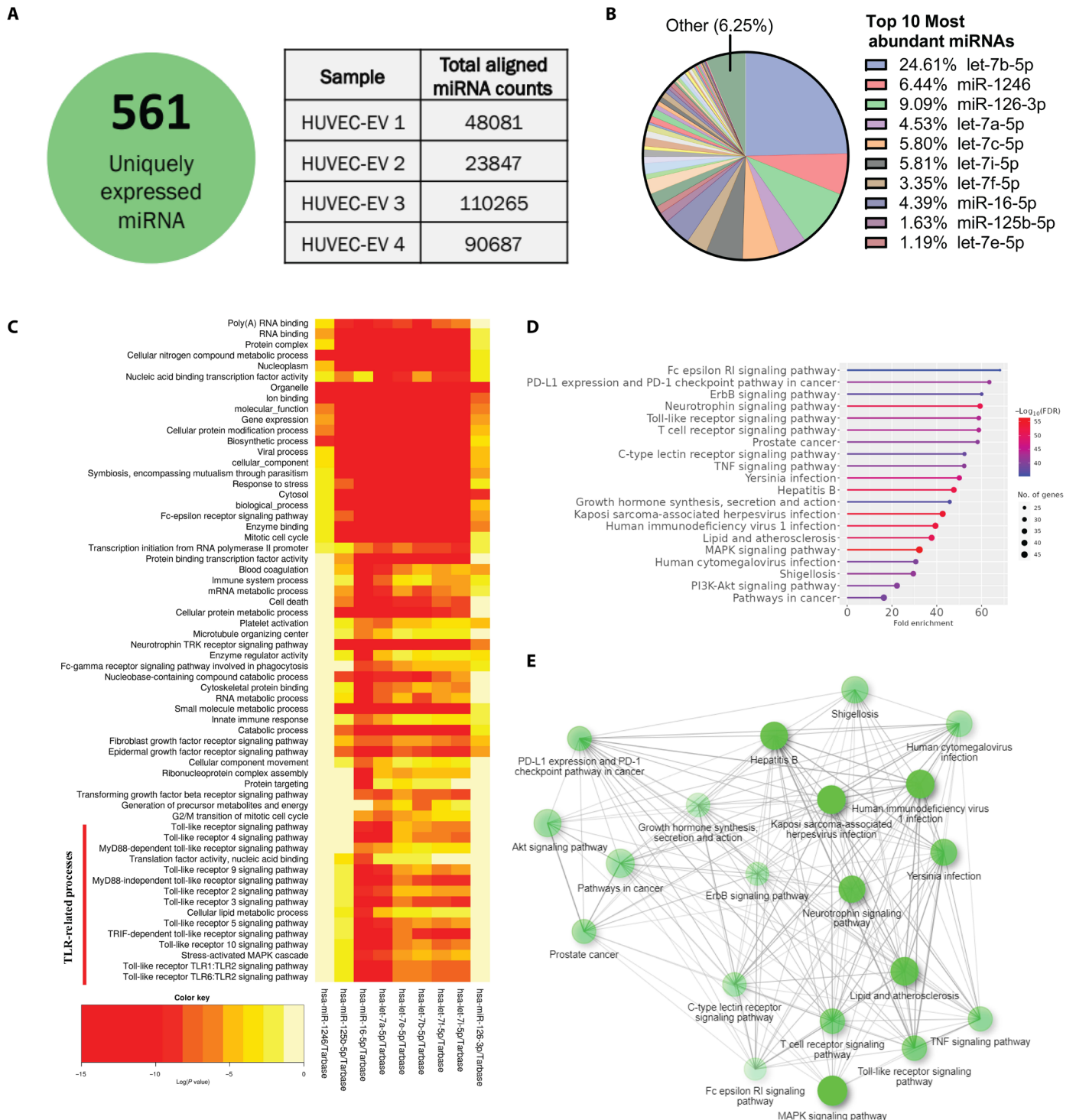
Fig. 5. miRNA sequencing reveals that HUVEC-EVs target TNF and TLR signaling pathways to mitigate proinflammatory response. (**A**) A diagram demonstrating the amount of uniquely expressed miRNAs in the HUVEC-EVs and their total aligned miRNA counts. (**B**) Fraction of 50 most-abundant miRNAs in HUVEC-EVs. (**C**) Heatmap of enriched biological processes for top nine most-abundant miRNA-derived from HUEV-EVs. (**E**) Kyoto Encyclopedia of Genes and Genomes (KEGG) pathway enrichment analysis for top nine most-abundant miRNAs in HUVEC-EVs. The y axis indicates the pathway name and the x axis indicates the enriched factors in each pathway. Bubble size indicates the number of genes. (**F**) The interaction of the top 20 significantly enriched KEGG pathways for the top nine abundant miRNAs in HUVEC-EV.
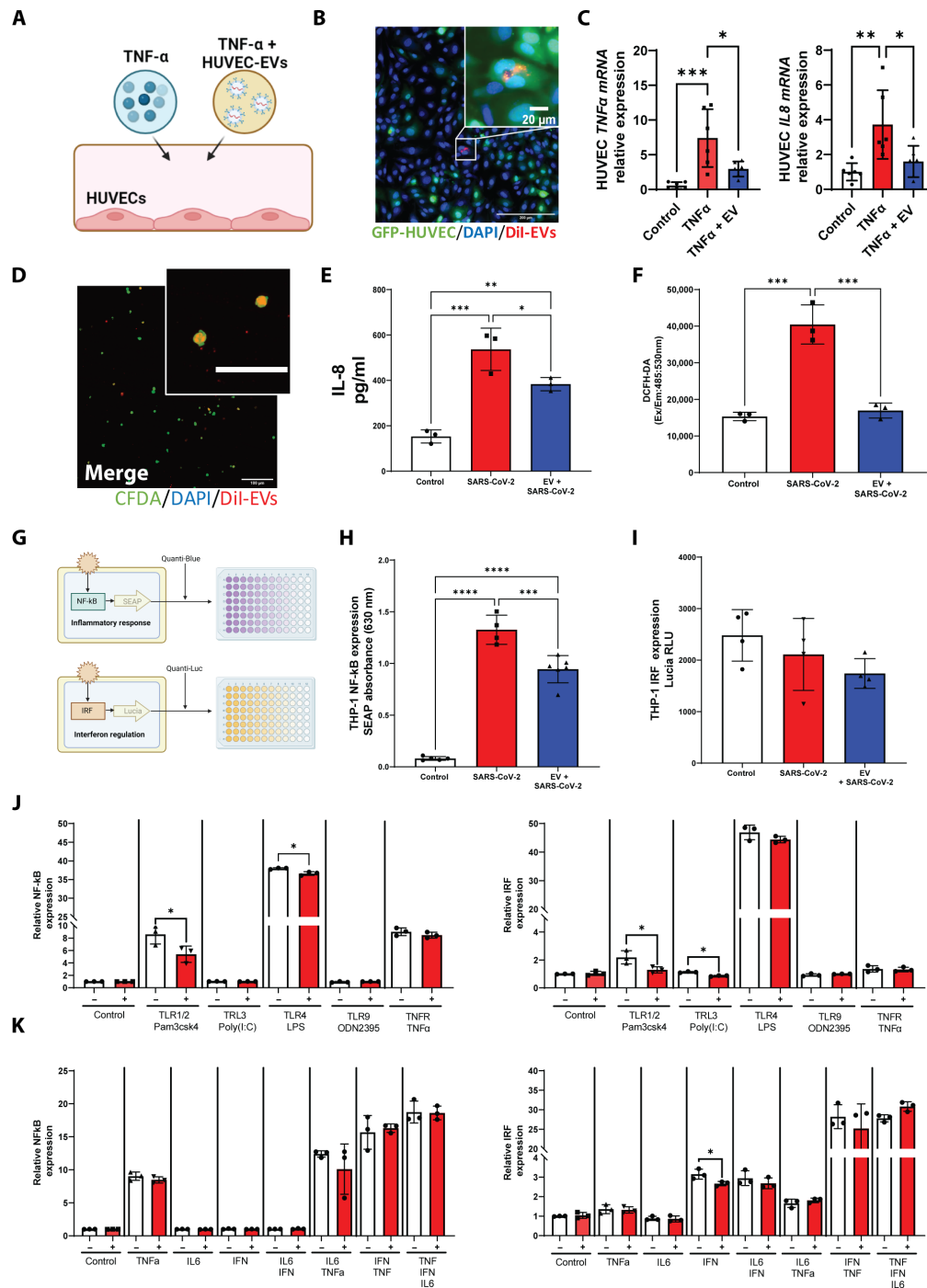
Fig. 6. HUVEC-EVs provide anti-inflammatory and cardioprotective effects through the TLR-NF-kB axis. (**A**) Schematic of experiments. HUVECs were stimulated with either TNF-α or TNF-α/HUVEC-EVs. (**B**) Representative confocal microscopy image of Dil-stained (red) EVs inside GFP-HUVECs. Scale bar, 200 μm. Magnified image scale bar, 20 μm. (**C**) Quantification of *TNFα* and *IL8* gene expression in HUVEC. $n = 6$. *$P < 0.05$, **$P < 0.01$, and ***$P < 0.001$. (**D**) Representative confocal images of Dil-stained HUVEC-EVs (red) inside PBMCs [green: carboxyfluorescein diacetate (CFDA)] Scale bar, 100 μm. Magnified image scale bar, 50 μm. (**E**) Extracellular ROS level. IL-8 secreted by PBMCs 24 hours after SARS-CoV-2 infection at MOI of 1. $n = 3$. *$P < 0.05$, **$P < 0.01$, and ***$P < 0.001$. (**F**) Extracellular ROS levels. $n = 3$. **$P < 0.01$ and ***$P < 0.001$. (**G**) Dual-reporter THP-1 cells used to monitor the NF-κB pathway and interferon-related factor (IRF) pathway were treated for 24 hours with SARS-CoV-2 at MOI of 1. Cell culture medium was assessed for (**H**) Secreted embryonic alkaline phosphate (SEAP) and (**I**) Lucia reporter activity. $n = 4$, ***$P < 0.001$, ****$P < 0.0001$. (**J**) Cells were stimulated with Pam3CSK (1 ng/ml; TLR1/2), 5 μM poly(l:C) (TLR3), lipopolysaccharide (LPS) (10 ng/ml; TLR4), 5 μM ODN2395 (TLR9), or TNF-α (1 ng/ml; TNFR). After 24 hours, NF-κB and IRF activation were assessed. $n = 3$ *$P < 0.05$. (**K**) THP-1 cells were first primed with EVs for 2 hours, then stimulated with IL-6 (1 ng/ml), IFN-γ (1 ng/ml), and/or TNF-α (1 ng/ml) and incubated for 24 hours. $n = 3$. *$P < 0.05$. All data are shown as means ± SD. One-way ANOVA with Bartlett's test in (C), (E), (F), (H), and (I). Student's *t* test with Bartlett's test in (J) and (K).

non-stimulated cells, confirming that SARS-CoV-2 infection activates NF-κB signaling (Fig. 6H). In contrast, IRF expression was not changed upon SARS-CoV-2 infection, consistent with the finding that SARS-CoV-2 antagonizes the interferon responses IFNAR1 lysosomal degradation (Fig. 6I) (*22*, *23*). Treatment with EVs before SARS-CoV-2 infection limited NF-κB activation (Fig. 6H), demonstrating that HUVEC-EVs mitigate inflammatory responses by inhibiting the NF-κB cascade.

A thorough screening of various innate sensors located upstream of NF-κB was then conducted to identify the specific EV-target receptors. NF-κB expression was significantly increased in THP-1 cells challenged with Pam3csk4 (an agonist of TLR1 and TLR2 heterodimer), lipopolysaccharide (LPS; TLR4 agonist), or TNF-α (an agonist of TLR) (Fig. 6J). Conversely, THP-1 cells primed with EVs before the addition of TLR agonist or TNF-α showed reduced Pam3csk and LPS-induced NF-κB activation, but similar levels of TNF-α–mediated NF-κB activation (Fig. 6J). Moreover, EVs were unable to suppress NF-κB activation when THP-1 cells were stimulated with individual cytokines (TNF-α, IL-6, and IFN-β) or a cocktail of cytokines (Fig. 6K), suggesting that EVs primarily target TLR-initiated inflammation and downstream factors. Collectively, these data show that EVs regulate proinflammatory responses of monocytes and shift activation toward an inflammatory resistance state, thereby mitigating local and systemic damage.

Extracellular vesicles reverse inflammation-induced cardiac dysfunction

Clinical data have demonstrated that patients infected with SARS-CoV-2 have elevated levels of IFN-γ, IL-6, and TNF-α (fig. S7) (*24*, *25*). This cytokine cocktail was applied here to a cardiac bundle termed Biowire in the absence of endothelial and immune cells, to benchmark the direct effects of EVs on the restoration of contractile function (fig. S8A). The application of cytokine cocktail led to a modest reduction in contractile force (fig. S8B) and maximum capture rate (fig. S8C), and to an increase in ET (fig. S8D), all of which correlate with cardiac dysfunction. HUVEC-EVs rescued dysfunctional cardiac tissues, as illustrated by a recovery of contraction force (fig. S8B) and tissue excitability (fig. S8D). Collectively, these data show that EVs can both reduce the magnitude of proinflammatory responses and contribute to directly preserving cardiomyocyte function in the inflammatory environment.

DISCUSSION

High fidelity, multi-cell–type, human in vitro models of inflammatory conditions of the myocardium remain scarce, ultimately slowing the progress toward new therapeutics. Considering COVID-19 as an example, among the 43 studies reviewed by Haussner *et al.* (*26*), treatment for COVID-19–associated myocarditis was highly variable, with low utilization. Cardiovascular involvement was first recognized in China, where patients with elevated serum levels of troponin I, IL-6, and other pro-natriuretic peptides were found to have an increased risk of mortality (*24*). Most therapeutic options still rely on the use of ACE inhibitors or beta-blockers, while treatments focusing on the immune system and subsequent systemic inflammatory response are scarce. Here, we developed a model of human SARS-CoV-2–induced myocarditis on-a-chip, demonstrating disease hallmarks such as the increased levels of cytokines triggered by the viral presence, which, in turn, further amplify cytokine release and the recruitment of circulating immune cells, thereby accelerating the progression of cardiac dysfunction (*27*–*29*). Microphysiological systems, such as the one described here, have limitations with respect to their ability to register sophisticated organ-level functional readouts such as ejection fraction. Correlations between in vitro contractility and in vivo ejection fraction may not be appropriate in all cases. Despite these limitations, insights into the effects of the virus and therapeutic interventions on the cardiac tissue can be obtained at a granularity that sometimes exceeds that of in vivo studies.

The application of SARS-CoV-2 to the vascularized cardiac tissue without immune cells did not cause an appreciable functional deficit in this study. Studies focusing on the direct cardiac infection of three-dimensional (3D) engineered cardiac tissue (i.e., in the models without vasculature and without immune cells), usually use a higher (up to 50 times) virus dosing to achieve a functional deficit. Some studies report the use of MOI of 10 and a prolonged observation period (144 hours after infection) (*30*). The reason for this is that cardiomyocytes express relatively low levels of ACE2 receptors. In the in vivo heart, most of the infection happens in non-myocytes including pericytes and fibroblasts (*31*).

Here, we used a more physiologically relevant virus dose (MOI of 0.1) with circulating immune cells to better recapitulate realistic loading in the body. This approach enabled us to develop a model of cytokine-mediated cardiovascular dysfunction, as systemic inflammation secondary to SARS-CoV-2 infection and subsequent infiltration of immune cells to the heart can indirectly damage cardiomyocytes and it is consistent with clinical observations (*15*).

Previously, we demonstrated that endothelial cells switch to a proinflammatory phenotype upon SARS-CoV-2 infection in the InVADE platform, as manifested by the elevated release of soluble vascular adhesion molecules (E-selectin and ICAM-1) and proinflammatory cytokines (angiopoietin-2, IL-6, IL-8, and TREM-1) (*20*). This endothelial cell activation promotes monocyte recruitment, leading to the activation of immune cells. The present study demonstrated that inflammation can also lead to the infiltration of monocytes and CD3 T lymphocytes, via the endothelium, into the cardiac parenchyma. This is consistent with the increased CD3^{+} T lymphocyte levels measured postmortem in the heart tissues of COVID-19 patients with myocarditis (*14*–*17*). Local infiltration of the immune cells results in an acute inflammatory response, causing the release of IL-8 and MCP-1 which further promotes monocyte recruitment to the site of inflammation. This, in turn, impairs cardiac function, consistent with the findings that immune cells are the primary cause of cardiac injury in patients with COVID-19 (*14*, *17*, *32*).

Some studies report that human PBMCs can be productively infected with SARS-CoV-2 (*33*), whereas other studies report a lack of productive infection in human cord blood-derived macrophages (*19*). In addition, viral protein has been reported to persist in human monocytes for up to 15 months after infection (*34*) and SARS-CoV-2 has been reported to persist in certain types of macrophages (e.g., lung) for prolonged time periods (*35*). These phenomena open the possibility for reinfection in a full system such as the one described here, which includes both cardiomyocytes and monocytes/macrophages that could worsen the contractile dysfunction beyond those caused by the inflammatory cytokines alone and may underpin the profound contractile deficit at a relatively low MOI of 0.1. Yet, our data indicate that, at MOI of 0.1, there was no acceleration of viral propagation in the CM + PBMC coculture, compared to the CM alone.

The heart is one of the most metabolically demanding organs and requires a large number of mitochondria to produce adenosine

5′-triphosphate (ATP). Here, excessive myocardial inflammation increased ccf-mtDNA presence, namely, ccf-mtND1 and ccf-mtND4 in the heart-on-a-chip model, which was also observed in patients diagnosed with COVID-19 admitted to the intensity care unit (ICU) with low LVEF (<50%). Several clinical studies found that patients with higher ccf-mtDNA concentrations are more likely to require intensive care and higher mortality (36, 37). Therefore, we suggest that ccf-mtDNA could be used as a biomarker to identify patients with COVID-19^{+} at risk of more serious LVEF dysfunction and predict clinical outcomes in ICU patients with COVID-19^{+}. Our findings are consistent with previous studies, which report that in the setting of cardiac injury, elevated levels of intracellular ROS triggered by proinflammatory cytokine activation led to mitochondrial membrane permeabilization and subsequent cell death (38). This cascade of events culminates in reduced expression of mitochondrial genes involved in oxidative phosphorylation, ATP metabolism, and mitochondrial transition (19), ultimately leading to mitochondrial dysfunction. The impaired mitochondria then release mtDNA as well as mitochondrial proteins (39), which may act as danger-associated molecular pattern that activate immune responses and elicit further damage (40, 41). Various inflammatory pathways, such as cGAS-STING and TLR4/9 and inflammasome formation, can lead to robust type I IFN responses and NF-κB–dependent proinflammatory responses, which may set off the apoptotic cascade (42).

These redundant and reinforcing inflammatory interactions in viral myocarditis pose a major challenge in pinpointing the critical cytokines/chemokines that drive the phenotype, necessitating a comprehensive strategy for inhibiting cytokine release. Several anti-inflammatory agents have shown clinical benefits in the acute management of COVID-19. For example, bromodomain and extraterminal family inhibitors (BETi) improved cardiac function in the LPS-induced mouse cytokine-storm model; however, loss of BET activity may negatively alter energy production in the mitochondria (43). Corticosteroids, such as dexamethasone, may also improve patient mortality, but systemic immunosuppression can impede viral clearance, thereby potentially exacerbating the disease (44–47).

Together, there remains a need for immunomodulatory compounds that can attenuate cytokine-induced cardiac dysfunction while preserving the mitochondrial energetics in patients with SARS-CoV-2–induced myocarditis. As endothelial cell–derived EVs have been shown to suppress immune cell activation (12) and alleviate cardiac cell death (10), this study tested the immunomodulatory potential of HUVEC-derived EVs to alleviate SARS-CoV-2–induced myocardial inflammation. HUVEC-EVs improved cardiac functionality after SARS-CoV-2 infection, as demonstrated by the recovery of electromechanical properties and mitigated release of ccf-mtDNA. miRNA-seq identified the let-7 family, miR-16, and miR-125b as the most abundant miRNA in HUVEC-EV cargo, which were predicted to target apoptotic processes, TLR signaling, and immune system processes. In addition, KEGG analysis demonstrated that the EVs target signaling pathways associated with TLR and TNF signaling pathways. Thus, EVs may provide therapeutic benefits by targeting genes associated with inflammation, thereby mitigating the production of proinflammatory cytokines. EV treatment of THP-1 reporter cells with monocyte-like phenotype-mitigated NF-κB, a central downstream transcriptional factor that governs inflammation and cellular stress, suppressed the TLR-mediated NF-κB activation observed following SARS-CoV-2 infection. This inhibition reduced the release of proinflammatory cytokines (IL-8) and mRNA levels of *Il-8* and *Tnf*-α, thereby impeding the activation of

NF-κB, and preventing positive feedback between cytokines and circulating monocytes. Given that TLR signaling is one of the enriched targets of HUVEC-EVs, the inhibition of this step is the preferred route to protect the heart against inflammatory injury.

There is evidence that exosomes produced by infected cells can affect virus propagation (48). Cells infected with viruses generate exosomes that are pivotal in facilitating interactions between cells that are infected and those that are not. The production and content of exosomes are influenced by SARS-CoV-2, which can manipulate the processes of exosome formation, secretion, and discharge to enhance its own infectiousness, transmissibility, and cellular dissemination (48). Here, we applied exosomes from healthy cells, therefore we do not believe this concern would be applicable.

Yet, the more cells uptake the exosomes, even therapeutic ones, the higher the chance they will uptake the virus since similar processes and cellular machinery are at play (48). It has been postulated that inhibition of exosome uptake by neighboring cells could attenuate virus spread (49, 50). This necessitates careful studies of the timing of exosome application in preclinical models to ultimately better inform clinical studies. A recent positive outcome from the phase 2 clinical trial on the use of mesenchymal stem cell–derived exosomes to attenuate acute respiratory distress syndrome in patients with COVID-19 further suggests that dosing and timing of exosome application can be successfully addressed for effective application in humans (51).

While we focused on the role of HUVEC-EVs in reducing immune cell activity and subsequent cytokine release to mitigate myocarditis in this study, several studies highlighted that miRNAs from EVs may also interfere with SARS-CoV-2 replication in the body (52–54). For example, Xie *et al.* (55) provided evidence that let-7 families, which are highly expressed in HUVEC-EVs, can suppress the expression of spike (S) and membrane (M) proteins, thereby suppressing viral-induced inflammation. It is possible that in addition to mediating anti-inflammatory effects on immune cells, miRNA encapsulated within EVs may bind to viral RNA, thereby inhibiting viral propagation.

Despite the detailed EV cargo analysis, a limitation of this study remains that no direct miRNA testing of the EV cargo was performed. Further studies, especially in highly defined microphysiological system preparations, could answer this question and a reasonable starting point would be an assessment of the miRNA effect on myocardial preparation alone since CMs are the main effectors of cardiac contractility.

Our results substantiate the hypothesis that circulating immune cells are probable contributors to myocardial dysfunction in the context of COVID-19. Nevertheless, the role of resident macrophages in contributing to cardiac pathology associated with this disease remains a major consideration and requires more understanding. Additional limitations of this work include relatively short observation time points, the absence of microvasculature in the parenchymal space, the need for a more precise and controlled inclusion of adaptive immunity, and systematic testing of the effects of the identified miRNAs.

In summary, COVID-19 is associated with an array of disease manifestations, including a massive inflammatory response that causes myocarditis. Here, we developed a vascularized heart-on-a-chip model of SARS-CoV-2–induced myocarditis to support therapeutics discovery and mechanistic studies. This work showed a tight correlation between elevated ccf-mtDNA and cardiovascular dysfunction in both a human-engineered myocarditis model and patients with COVID-19.

The increase was traced back to proinflammatory mediators stimulated by the TLR pathway. Therefore, a therapeutic option targeting TLR may present an important and viable approach to reducing SARS-CoV-2–induced myocarditis and to improve patient outcomes. The ability of HUVEC-EVs to inhibit TLR-mediated NF-κB activation, thereby reducing myocardial inflammation and mitochondrial damage and improving cardiac function, was demonstrated. Future studies characterizing the activities of miRNAs in HUVEC-EVs will help determine effective means of deactivating SARS-CoV-2–induced inflammation.

MATERIALS AND METHODS
InVADE platform fabrication
The InVADE platform was prepared as we described previously (27–29). Briefly, the fabrication of the silicon master mold involved the use of the standard soft lithography technique, with photomasks designed using AutoCAD software. To prepare the polydimethylsiloxane (PDMS) molds, a mixture of 10 parts silicon elastomer and 1 part curing agent (Sylgard 184, Dow Corning) was prepared. PDMS molds were made by replica molding from the SU-8 mold. Subsequently, a biocompatible ultraviolet (UV)–cross-linkable elastomeric polymer known as poly(octamethylene maleate (anhydride) citrate) (POMaC), consisting of a combination of 1,8-octanediol, citric acid, and maleic anhydride, mixed with poly(ethylene glycol) dimethyl ether (PEG-DM) porogen at a 6:4 (POMaC:PEGDM, wt/wt) ratio, along with 5% 2-hydroxy-1-[4(hydroxyethoxy)phenyl]-2-methyl-1-propane (Irgacure 2959; Sigma-Aldrich) photoinitiation, was perfused through PDMS channels of the master mold. Through exposure to a UV light source, scaffolds with a square luminal structure and lid were cross-linked. The top and bottom features were then bonded together using a 3D stamping technique as we previously described (27–29), to create a perfusable microvessel, termed Angitube patterned with microholes (15 μm by 15 μm) spaced at 15 μm apart as we described (28). The Angiotube scaffolds with an inner luminal dimension of 100 μm and wall thickness of 50 μm were then placed onto a patterned hot-embossed polystyrene base plate that had a footprint of a 96-well plate, and the plate was bonded onto a bottomless 96-well plate using polyurethane glue (GS Polymers). By fitting the Angiotube microvessel into groves of the patterned hot-embossed base, it is possible to connect three wells in one column of a 96-well plate. The three wells become a unit for cell cultivation. Before starting cell culture experiments, the entire plate underwent sterilization by treating it with 70% filtered ethanol for 2 hours at room temperature.

Cell culture
HUVECs were cultured and maintained in endothelial cell growth medium (EGM-2, PromoCell) under standard cell culture conditions, with 5% CO_2 at 37°C. To endothelialize the polymeric lumen of the InVADE system, 0.2 wt % bovine gelatin (type A; Sigma-Aldrich) was coated for 1.5 hours onto the POMAC microvessel, followed by overnight EGM-2 medium conditioning. For endothelialization of the Angiotube, 5 μl of concentrated endothelial cell suspension (25×10^6 cells/ml) were seeded at both inlet and outlet, allowing endothelial cells to be packed inside the lumen for 1.5 hours at 37°C. Unattached endothelial cells were then flushed by adding EMG-2 media into the inlet to initiate perfusion.

Ventricular cardiomyocytes were derived from human iPSC line BJ1D using a monolayer differentiation protocol, as previously described (56). To generate cardiac tissue on the InVADE platform or Biowire system described below, human iPSC–derived cardiomyocytes were suspended in fibrinogen from human plasma (Sigma-Aldrich) at a concentration of 50×10^6 cells/ml. Then, 1 μl of thrombin from human plasma was added to 3.5 μl of the cardiomyocyte-human fibrinogen mixture (Sigma-Aldrich). Then, 3 μl of the mixture containing cardiomyocytes was placed onto the InVADE bioscaffold. The cardiomyocyte mixture was then allowed to undergo cross-linking for 10 min at 37°C. The following medium was used for cardiac tissue maintenance: Induction 3 Medium (I3M): stepPro-34 media serum-free medium (Gibco), 20×10^{-3}M Hepes (Gibco), 1% GlutaMAX (Gibco), 1% penicillin-streptomycin (Gibco), and 2-phosphate ascorbic acid (213 μg/ml; Sigma-Aldrich) containing aprotinin from bovine lung (1:1000 dilution) (Sigma-Aldrich). Perfusion in this system is achieved by a hydrostatic pressure gradient, in which 500 μl of EGM-2, 350 μl of I3M, and 20 μl of EGM-2 media were added to the inlet, tissue chamber, and outlet of the InVADE system, respectively. The continuous flow in the scaffold is maintained by placing the InVADE system on a rocker (Perfusion Rocker Mini, MIMETAS) with a 20° tilt that is automated to reverse the flow every 4 hours. The endothelial media perfuses the microvessel by moving between the inlet and outlet well via a gravity-driven flow. This is estimated to achieve a flow rate of 1.4 μl/min and a shear stress of 1.3 dyne/cm² according to our previous studies (20, 28). The tissue well contains cardiac media to support iPSC-derived cardiomyocytes.

Human PBMCs were obtained from STEMCELL Technologies (catalog no. 700.25.1). PBMCs were cultured and maintained in RPMI 1640 with 10% fetal bovine serum (FBS) and 1% penicillin-streptomycin under standard cell culture conditions, with 5% CO_2 at 37°C. THP-1 dual-reporter cells (InvivoGen) were cultured and maintained in Roswell Park Memorial Institute (RPMI) 1640 with 10% heat-inactivated FBS, 1% normocin, and 1% penicillin-streptomycin under standard cell culture conditions, with 5% CO_2 at 37°C.

Viral infection
All handling of SARS-CoV-2/SB2 was conducted in the combined containment level 3 (C-CL3) unit at University of Toronto. SARS-COV-2 was expanded in Vero E6 cells. Viral dosing was defined by TCID50 in Vero E6 cells. Before the viral infection, both the endothelial cell compartment and the cardiac tissue compartment were washed with serum-free Eagle's minimum essential medium (EMEM) media, then media was replaced with serum-free EMEM containing SARS-CoV-2 at MOI of 0.1 and perfused through the endothelial cell compartment for 90 min. Virus-containing media were replaced by EGM2 and I3M media for the endothelial cell compartment and cardiac tissue compartment, respectively. PBMCs were suspended in EGM-2 media at a concentration of 300,000 cells/ml, and 500 μl of EGM-2 containing PBMCs was applied by perfusion from the inlet for the InVADE experiment after viral infection.

Viral RNA extraction and viral titer quantification in cocultures of CM and PBMCs
A total of 7×10^5 BJ1D stem cell–derived cardiomyocytes were seeded in a 24-well plate with an 8-μm Transwell insert. Base plates were coated with 1:10 diluted growth factor reduced Matrigel in Iscove's modified Dulbecco's medium. Cardiomyocyte monolayers were kept at 37°C for 5 days before viral infection. Vero E6 cells were seeded on the 24-well plates as a positive control for viral replication 1 day before the infection. On the day of the viral infection, 5×10^5 PBMCs were

added to the Transwell for the cardiomyocyte-PBMC group. Cells were treated with the virus for 90 min in media without FBS at an MOI of 1. Media containing the virus were removed and fresh media were added to the wells. Media were collected at each time point and kept frozen in a −80°C freezer. Viral RNA extraction was performed by PureLink viral RNA/DNA extraction kit. cDNA was synthesized with SuperScript II reverse transcription enzyme. Quantitative PCR was performed on the cDNA sample using SYBR Green reagent with the following primers: forward 5′-ATTGTTGATGAGCCTGAAG-3′, reverse 5′-TTCGTACTCATCAGCTTG-3′. For the standard, serial dilution of known concentration of virus RNA extract was prepared and the absolute viral particles were calculated by extrapolating the standard curve.

Immunostaining

SARS-CoV-2–infected samples were fixed with 10% formalin for 1 hour at room temperature, as recommended by C-CL3 safety protocol. Subsequently, samples were washed three times with PBS, and then blocked with PBS containing 10% FBS and 0.1% Triton X-100, at 4°C overnight. The tissues were then incubated with primary mouse monoclonal anti-human cardiac troponin T (Thermo Fisher Scientific) or mouse monoclonal anti-human CD3 (Thermo Fisher Scientific), at 4°C, overnight. The samples were then washed three times with PBS for 15 min, incubated with anti-mouse Alexa Fluor 488 (Life Technologies) and anti-mouse Alexa Fluor 647 (Abcam) secondary antibody, overnight, at 4°C, and then rinsed three times with PBS. For PBMC identification, it was tagged with CellTracker dye CM-DiI according to the manufacturer's protocol. Immunofluorescence images were captured with a confocal fluorescence microscope (Nikon A1R).

Cytokine analysis

I3M medium was collected from the cardiac tissue compartment of the InVADE platform after viral infection. SARS-CoV-2 in the collected medium was inactivated by the addition of 1% Triton X-100 for 1 hour, in accordance with the CL-3 facility safety protocol. Samples were then centrifuged at 500g for 10 min and 30 μl of supernatant was collected for proinflammatory cytokine/chemokine analysis. The concentrations of IL-1α, IL-1β, IL-4, IL-6, IL-8, IL-10, IL-13, MCP-1, IFN-γ, and TNF-α were measured using the Quantibody Human Inflammation Array (RayBiotech, USA), according to the manufacturer's protocol. The fluorescence was analyzed using GenePix Professional 4200 Microarray Scanner at 530 nm.

Functional assessment of cardiac tissue

After 72 hours of SARS-CoV-2 infection, contractile activity of cardiac tissue was assessed by measuring activity in response to electrical field stimulation using an external stimulator (CStype 223, Hugo Sachs electronics-Havard apparatus). ET was first measured, followed by measuring the displacement of micro-cantilevers from a video recorder in the CL-3 facility at 30 frames at 2× ET at 1 Hz. Relative changes in intracellular calcium concentrations were determined by adding Fluo-4 NW (Thermo Fisher Scientific) to the cardiac tissue compartment for 30 min, at 37°C. Intracellular calcium transients were recorded at 30 frames at 2× ET under green light a channel ($\lambda_{ex}/ \lambda_{em}$ = 490/525 nm) at 1 Hz. Videos are then analyzed using ImageJ Software (National Institutes of Health). The calcium transient amplitude and kinetics of the calcium signals were analyzed using a customized MATLAB code as previously described

(57). The ratio of peak tissue fluorescence intensity, dF/F_0, was calculated to determine the relative changes in intracellular Ca^{2+}. The contractile measurements were determined using the ImageJ Spot-Tracker plugin. A fluorescent microscope (EVOS, Life Technologies) was used to record videos in the CL-3 facility.

Study participant and data collection

This study was approved by the Unity Health Toronto Research Ethics Board (REB no. 20-078). Forty patients with acute respiratory failure and suspicion of COVID-19 who admitted to medical-surgical ICUs in Toronto, Canada, between March 2020 and March 2022 and enrolled in the COVID-19 Longitudinal Biomarkers of Lung Injury (COLOBILI) study. The infection status of admitted patients was confirmed prospectively by SARS-CoV-2 PCR tests and by antigen testing. The demographic characteristics (age), cardiac examination (LVEF, left ventricle size, right ventricle size, systolic function, and diastolic function), and clinical laboratory values (pH, pO2, and lactate) were recorded, along with the synchronous collection of blood samples. Human samples were obtained with informed consent. The cohort of 40 patients was categorized into two different groups: patients with SARS-CoV-2–negative requiring ICU care ($n = 20$) and patients with SARS-CoV-2–positive requiring ICU care ($n = 20$).

Circulating cell-free mitochondrial DNA measurement

mtDNA was extracted from 100 μl cell supernatant and 50 μl patient plasma samples following the manufacturer's protocol provided with the QiaAMP DNA mini kit (Qiagen). Extracted DNA was eluted with Ultra-Pure Distilled DNAse-free and RNAse-free Water (Invitrogen): 50 μl for cell supernatant and 100 μl for patient plasma. A commercially synthesized oligonucleotide of the PCR product (Integrated DNA Technologies), of known concentration, was serially diluted to a concentration ranging from 10^8 to 10^2 copies/μl and used to estimate the absolute concentration of ccf-mtDNA. Mitochondrial genes, ND4 and ND1, were used to represent the major and minor arc of the mitochondrial genome. TaqMan Duplex PCR was run on BioRad's C1000 Thermal cycle CFX96 Real-Time System using 20 μl of reaction mixture including 10 μl of TaqMan Fast Advanced Master Mix (Thermo Fisher Scientific), 4 μl of DNA, 1 μl each of forward and reverse primers, and 1 μl of TaqMan probe for each gene. qPCR cycling conditions were as follows: 50°C for 2 min, 95°C for 20 s, 40 cycles of 95°C for 3 s, and 60°C for 30 s, followed by a fluorescence read per cycle.

Primer/probe sequence.

ND4- F1 5′-CCATTCTCCTCCTATCCCTCAAC-3′.

ND4- R1 5′-ACAATCTGATGTTTTGGTTAAACTATATTT-3′.

ND4- Probe 5′-FAM/CCGACATCA/ZEN/TTACCGGGTTTT CCTCTTG/3IABkFQ/-3′.

ND1- F1 5′-CCCTAAAACCCGCCACATCT-3′.

ND1- R1 5′-GAGCGATGGTGAGAGCTAAGGT-3′.

ND1- Probe 5′-HEX/CCATCACCC/ZEN/TCTACATCACC-GCCC/3IABkFQ/-3′.

ND4 + ND1 GeneBlock 5′-

C A C G A G A A A A C A C C C T C A T G T T C A T A - CACCTATCCCCCATTCTCCTCCTATCCCTCAACCCCGACAT- CATTACCGGGTTTTCCTCTTGTAAATATAGTTTAACCAAAA- CATCAGATTGTGAATCTGACAACAGAGGCTCTCTTCACCAA- AGAGCCCCTAAAACCCGCCACATCTACCATCACCCTCTA- CATCACCGCCCCGACCTTAGCTCTCACCATCGCTCTTCTAC- TATGAACCCCCCTCCCCATACCCAA-3′.

EV isolation and analysis

EVs were isolated using the miRCRY exosome isolation kit (Qiagen), according to the manufacturer's protocol. Briefly, 80% confluent HUVECs were washed once with PBS and switched to a fresh serum-free culture medium, which was collected 48 hours thereafter. The conditioned medium was centrifuged at 3200g for 10 min to remove cell debris. The supernatant was collected and 400 µl of exosome isolation reagent was added to 1 ml of media to allow EVs to precipitate overnight, at 4°C. The supernatant was discarded. Pellets were resuspended with PBS without mixing to wash off the exosome isolation reagent, then centrifuged for 1 min at 3200g. The supernatant was then carefully aspirated. Precipitated EVs were reconstituted in PBS and the concentration and size distribution of 1× diluted EV samples were determined by NTA via NanoSight (Malvern). For all HUVEC-EV treatment studies, 2.5×10^8 EVs were added to 1 ml of cell culture medium.

Western blotting

Western blotting was performed using the ExoA Antibody Kit according to the manufacturer's protocol (System Biosciences, USA). Immunoblots were cut before primary antibody hybridization. Immunopositive bands were detected using the ECL Plus Kit (Invitrogen, USA), according to the manufacturer's protocol. Antibodies were used at the following concentration: anti-CD9 (1:500; Cell Signaling Technology), anti-CD63 (1:500; Abcam), anti-calnexin (1:500; Abcam), and anti–flotillin-1 (1:500; Cell Signaling Technology). The images provided are the largest view saved from image acquisition.

Transmission electron microscopy

EV pellets, isolated as described above, were suspended in 4% electron microscopy-grade paraformaldehyde in sodium phosphate buffer. EVs (10 µl) were placed on square carbon electron microscopy grids for 20 min, after which the excess solution was washed off with filter paper. The sections were stained with saturated uranyl acetate for 5 min and rinsed in distilled water, followed by Reynold's lead citrate solution for 5 min. To image cardiac tissue sections, cardiac tissues were fixed with 10% formalin and 1% glutaraldehyde in 0.1 M PBS for 1 hour at room temperature. The samples were then fixed in 1% osmium tetraoxide in PBS for 1 hour at room temperature, in the dark. Cardiac tissues were dehydrated using an ethanol series of 30, 50, 80, and 95%, each for 5 min. The samples were then transferred into 100% ethanol three times for an additional 10 min, at room temperature, for complete dehydration. The samples were then washed twice with propylene oxide for 30 min, and then embedded in epoxy resin. After the polymerization, the solid resin blocks were sectioned on a Reichert Ultracut E-microtome to 90 nm thickness and collected on 200-mesh copper grids. The sections were stained with saturated uranyl acetate and Reynold's lead citrate solution for 15 min and then photographed with a Hitachi H7000 transmission electron microscope at an acceleration voltage of 80 to 120 kV.

EV miRNA sequencing

EVs were isolated from HUVEC-conditioned medium, as described above. EV pellets were lysed, and total RNA was isolated using the miRNeasy Micro Kit (Qiagen, catalog no. 217084), according to the manufacturer's protocol. Total RNA was sent to Novogene for DNase treatment and subsequent preparation for sequencing. Briefly, treated total RNA was quantified using the Qubit RNA HS assay (Thermo Fisher Scientific), and the quality was measured using the Bioanalyzer 2100 Eukaryote Total RNA Nano assay (Agilent Technologies, CA, USA). Libraries were prepared using the QIAseq miRNA Library Kit (Qiagen, catalog no. 331502) and then sequenced using a NovaSeq S4 (Illumina) at a read length of 2× 150 base pairs (bp) and an average depth of 12 million reads. R1 reads were trimmed to 75 bp before analysis. Using the Qiagen RNA-seq Analysis Portal 3.0 (workflow version 1.2), trimmed R1 sequencing data were aligned to the human genome (GRCh38.103) via the miRbase v22 database. miRNA count files were extracted for further analysis.

EV labeling and uptake by the cells

EV suspensions were incubated with 2 µM CellTracker dye CM-DiI (Invitrogen) in Hank's balanced salt solution for 5 min, at 37°C, and subsequently placed on ice for an additional 15 min. Excess dye was removed using an exosome spin column (MW 100,000), as per the manufacturer's instructions. For uptake analysis, stained EVs from 0.5 ml of medium (approximately 0.5×10^9 EVs) were cultured with HUVECs and PBMCs for 2 hours. Cells were then rinsed twice with PBS, and then fixed with 4% paraformaldehyde. Immunofluorescence images were captured with a confocal fluorescence microscope (Nikon A1R).

TLR agonist stimulation using THP-1

THP-1 dual-reporter cells (1×10^5 cells per well in round bottom 96-well plates) were treated with a TLR agonist in combination with HUVEC-EVs: diprovocim-1 (1 ng/ml; TLR1/2), poly(I:C) (2 µg/ml; TLR3), LPS (10 ng/ml; TLR4), 2 µM ODN2395 (TLR9), and TNF-α (1 ng/ml). For the cytokine study, cytokines were added individually or in combination with HUVEC-EVs: IL-6 (1 ng/ml), TNF-α (1 ng/ml), and IFN-γ (1 ng/ml). After a 24-hour incubation, NF-κB and IRF activation were assessed by measuring the levels of SEAP and Lucia luciferase using Quanti-Blue and Quanti-Luc, respectively. SEAP levels were measured by reading optical density at 650 nm. Lucia luciferase levels were determined by measuring the relative light units in a luminometer. HUVEC-EVs were added 2 hours before cytokine stimulation to determine the roles of EVs in modulating NF-κB and IRF activation.

Measurement of extracellular ROS

A total of 1×10^5 cells PBMCs were cultured in a round bottom 96-well plate. PBMCs were then infected with SARS-CoV-2 at MOI of 1 for 24 hours. To determine the role of EVs in modulating ROS generation, EVs were added 2 hours before SARS-CoV-2 infection. Release of extracellular ROS was measured by plating cell culture supernatant in black 96-well plates, adding 2,7-dichlorofluoroscein acetate, and incubating at room temperature. Fluorescence was read at 488-nm excitation and 525-nm emission.

Proinflammatory cytokine/chemokine stimulation of 3D cardiac tissues

Biowire cardiac tissues were prepared as previously described (57, 58). Briefly, the Biowire platform consists of two parallel POMAC wires (100 mm in diameter) placed at the opposing ends of ~5 mm long, 1 mm wide microwell hot embossed into tissue culture polystyrene. To generate cylindrical cardiac tissue, human iPSC–derived cardiomyocytes were suspended in fibrinogen from human plasma (Sigma-Aldrich) at a concentration of 50×10^6 cells/ml. Then, 1 µl of thrombin from human plasma was added to 3.5 µl of the cardiomyocyte-human fibrinogen mixture (Sigma-Aldrich) and 2 µl of the mixture was carefully pipetted into the microwell. The tissues were cultured for 7 days to allow for remodeling and tissue compaction in the presence of

cardiac media described above. Subsequently, three tissue samples were placed in 12-well plates, each containing 1 ml of I3M) media. Recombinant TNF-α, IFN-γ, IL-6, and/or IL-8 (purchased from PeproTech) were added at a concentration of 10 ng/ml. A total of 2.5×10^8 EVs were cotreated with cytokine cocktails to determine the roles of EVs in modulating cardiac tissue functions. Cardiac tissue functions, including ET, maximum capture rate, and contraction force, were measured 6 hours after the cytokine addition using an Olympus CKX41 inverted microscope and CellSense Software. These measurements are performed under electrical pacing at 1 Hz, via a pair of carbon electrodes (3.2mm in diameter, Ladd Research Industries) supplied by an external stimulator (Grass 88x) as we described in detail previously (*57*). The autofluorescent properties of POMAC wires allow for the determination of force of contraction by tracking the displacement of the polymer wire at the center and conversion of displacement into force via calibration curves as we previously described. The displacement was measured from fluorescent videos captured at 100 frames per second using what CMOS camera and Olympus CKX41 inverted microscope and processed from individual frames using the ImageJ SpotTracker plugin. The force was calculated from displacement via calibration curves using a customized MATLAB code as previously described (*57*).

LDH assay

The amount of lactate dehydrogenase (LDH) released by the cardiac tissues was analyzed with a Cayman LDH cytotoxicity assay kit (Cayman), as per the manufacturer's protocol.

Data and statistical methods

GraphPad Prism version 9.0a was used for all statistical analyses and to generate plots. Data are reported as means ± SD. Significant differences between groups were analyzed by analysis of variance (ANOVA) with Bartlett's test multiple comparison test and Student's t test, where appropriate. Differences at $P < 0.05$ were considered statistically significant.

Supplementary Materials

This PDF file includes:
Figs. S1 to S8
Legend for data file S1

Other Supplementary Material for this manuscript includes the following:
Data file S1

REFERENCES AND NOTES

1. E. Y. Wang, N. Rafatian, Y. Zhao, A. Lee, B. F. L. Lai, R. X. Lu, D. Jekic, L. D. Huyer, E. J. Knee-Walden, S. Bhattacharya, P. H. Backx, M. Radisic, Biowire model of interstitial and focal cardiac fibrosis. *Acs. Central. Sci.* **5**, 1146–1158 (2019).

2. E. Y. Wang, U. Kuzmanov, J. B. Smith, W. Dou, N. Rafatian, B. F. L. Lai, R. X. Z. Lu, Q. Wu, J. Yazbeck, X.-O. Zhang, Y. Sun, A. Gramolini, M. Radisic, An organ-on-a-chip model for pre-clinical drug evaluation in progressive non-genetic cardiomyopathy. *J. Mol. Cell. Cardiol.* **160**, 97–110 (2021).

3. O. Mastikhina, B.-U. Moon, K. Williams, R. Hatkar, D. Gustafson, O. Mourad, X. Sun, M. Koo, A. Y. L. Lam, Y. Sun, J. E. Fish, E. W. K. Young, S. S. Nunes, Human cardiac fibrosis-on-a-chip model recapitulates disease hallmarks and can serve as a platform for drug testing. *Biomaterials* **233**, 119741 (2020).

4. S. Lukassen, R. L. Chua, T. Trefzer, N. C. Kahn, M. A. Schneider, T. Muley, H. Winter, M. Meister, C. Veith, A. W. Boots, B. P. Hennig, M. Kreuter, C. Conrad, R. Eils, SARS-CoV-2 receptor ACE2 and TMPRSS2 are primarily expressed in bronchial transient secretory cells. *EMBO J.* **39**, e105114 (2020).

5. J. Lan, J. Ge, J. Yu, S. Shan, H. Zhou, S. Fan, Q. Zhang, X. Shi, Q. Wang, L. Zhang, X. Wang, Structure of the SARS-CoV-2 spike receptor-binding domain bound to the ACE2 receptor. *Nature* **581**, 215–220 (2020).

6. H. Xu, G. Liu, J. Gong, Y. Zhang, S. Gu, Z. Wan, P. Yang, Y. Nie, Y. Wang, Z. Huang, G. Luo, Z. Chen, D. Zhang, N. Cao, Investigating and resolving cardiotoxicity induced by COVID-19 treatments using human pluripotent stem cell-derived cardiomyocytes and engineered heart tissues. *Adv. Sci.* **9**, 2203388, (2022).

7. A. Sharma, G. Garcia, Y. Wang, J. T. Plummer, K. Morizono, V. Arumugaswami, C. N. Svendsen, Human iPSC-derived cardiomyocytes are susceptible to SARS-CoV-2 infection. *Cell Rep. Med.* **1**, 100052 (2020).

8. J. A. Perez-Bermejo, S. Kang, S. J. Rockwood, C. R. Simoneau, D. A. Joy, A. C. Silva, G. N. Ramadoss, W. R. Flanigan, P. Fozouni, H. Li, P.-Y. Chen, K. Nakamura, J. D. Whitman, P. J. Hanson, B. M. McManus, M. Ott, B. R. Conklin, T. C. McDevitt, SARS-CoV-2 infection of human iPSC–derived cardiac cells reflects cytopathic features in hearts of patients with COVID-19. *Sci. Transl. Med.* **13**, eabf7872 (2021).

9. R. Kalluri, V. S. LeBleu, The biology, function, and biomedical applications of exosomes. *Science* **367**, (2020).

10. M. Yadid, J. U. Lind, H. A. M. Ardoña, S. P. Sheehy, L. E. Dickinson, F. Eweje, M. M. C. Bastings, B. Pope, B. B. O'Connor, J. R. Straubhaar, B. Budnik, A. G. Kleber, K. K. Parker, Endothelial extracellular vesicles contain protective proteins and rescue ischemia-reperfusion injury in a human heart-on-chip. *Sci. Transl. Med.* **12**, eaax8005 (2020).

11. B. Liu, B. W. Lee, K. Nakanishi, A. Villasante, R. Williamson, J. Metz, J. Kim, M. Kanai, L. Bi, K. Brown, G. D. Paolo, S. Homma, P. A. Sims, V. K. Topkara, G. Vunjak-Novakovic, Cardiac recovery via extended cell-free delivery of extracellular vesicles secreted by cardiomyocytes derived from induced pluripotent stem cells. *Nat. Biomed. Eng.* **2**, 293–303 (2018).

12. M.-S. Njock, H. S. Cheng, L. T. Dang, M. Nazari-Jahantigh, A. C. Lau, E. Boudreau, M. Roufaiel, M. I. Cybulsky, A. Schober, J. E. Fish, Endothelial cells suppress monocyte activation through secretion of extracellular vesicles containing antiinflammatory microRNAs. *Blood* **125**, 3202–3212 (2015).

13. N. G. dela Paz, P. A. D'Amore, Arterial versus venous endothelial cells. *Cell Tissue Res.* **335**, 5–16 (2009).

14. C. Basso, O. Leone, S. Rizzo, M. D. Gaspari, A. C. van der Wal, M.-C. Aubry, M. C. Bois, P. T. Lin, J. J. Maleszewski, J. R. Stone, Pathological features of COVID-19-associated myocardial injury: A multicentre cardiovascular pathology study. *Eur. Heart J.* **41**, ehaa664 (2020).

15. G. Tavazzi, C. Pellegrini, M. Maurelli, M. Belliato, F. Sciutti, A. Bottazzi, P. A. Sepe, T. Resasco, R. Camporotondo, R. Bruno, F. Baldanti, S. Paolucci, S. Pelenghi, G. A. Iotti, F. Mojoli, E. Arbustini, Myocardial localization of coronavirus in COVID-19 cardiogenic shock. *Eur. J. Heart Fail.* **22**, 911–915 (2020).

16. D. Lindner, A. Fitzek, H. Bräuninger, G. Aleshcheva, C. Edler, K. Meissner, K. Scherschel, P. Kirchhof, F. Escher, H.-P. Schultheiss, S. Blankenberg, K. Püschel, D. Westermann, Association of cardiac infection with SARS-CoV-2 in confirmed COVID-19 autopsy cases. *JAMA Cardiol.* **5**, 1281–1285 (2020).

17. M. Bearse, Y. P. Hung, A. J. Krauson, L. Bonanno, B. Boyraz, C. K. Harris, T. L. Helland, C. F. Hilburn, B. Hutchison, S. Jobbagy, M. S. Marshall, D. J. Shepherd, J. A. Villalba, I. Delfino, J. Mendez-Pena, I. Chebib, C. Newton-Cheh, J. R. Stone, Factors associated with myocardial SARS-CoV-2 infection, myocarditis, and cardiac inflammation in patients with COVID-19. *Modern Pathol.* **34**, 1345–1357 (2021).

18. X. Yao, T. Li, Z. He, Y. Ping, H. Liu, S. Yu, H. Mou, L. Wang, H. Zhang, W. Fu, T. Luo, F. Liu, Q. Guo, C. Chen, H. Xiao, H. Guo, S. Lin, D. Xiang, Y. Shi, G. Pan, Q. Li, X. Huang, Y. Cui, X. Liu, W. Tang, P. Pan, X. Huang, Y. Ding, X. Bian, A pathological report of three COVID-19 cases by minimal invasive autopsies. *Chin. J. Pathol.* **49**, 411–417 (2020).

19. A. L. Bailey, O. Dmytrenko, L. Greenberg, A. L. Bredemeyer, P. Ma, J. Liu, V. Penna, E. S. Winkler, S. Sviben, E. Brooks, A. P. Nair, K. A. Heck, A. S. Rali, L. Simpson, M. Saririan, D. Hobohm, W. T. Stump, J. A. Fitzpatrick, X. Xie, X. Zhang, P.-Y. Shi, J. T. Hinson, W.-T. Gi, C. Schmidt, F. Leuschner, C.-Y. Lin, M. S. Diamond, M. J. Greenberg, K. J. Lavine, SARS-CoV-2 infects human engineered heart tissues and models COVID-19 myocarditis. *Jacc Basic Transl. Sci.* **6**, 331–345 (2021).

20. R. X. Z. Lu, B. F. L. Lai, N. Rafatian, D. Gustafson, S. B. Campbell, A. Banerjee, R. Kozak, K. Mossman, K. L. Howe, J. E. Fish, M. Radisic, Vasculature-on-a-chip platform with innate immunity enables identification of angiopoietin-1 derived peptide as a therapeutic for SARS-CoV-2 induced inflammation. *Lab Chip* **22**, 1171–1186 (2022).

21. L. Fu, B. Wang, T. Yuan, X. Chen, Y. Ao, T. Fitzpatrick, P. Li, Y. Zhou, Y. Lin, Q. Duan, G. Luo, S. Fan, Y. Lu, A. Feng, Y. Zhan, B. Liang, W. Cai, L. Zhang, X. Du, L. Li, Y. Shu, H. Zou, Clinical characteristics of coronavirus disease 2019 (COVID-19) in China: A systematic review and meta-analysis. *J. Infection* **80**, 656–665 (2020).

22. R. S. Freitas, T. F. Crum, K. Parvatiyar, SARS-CoV-2 spike antagonizes innate antiviral immunity by targeting interferon regulatory factor 3. *Front. Cell Infect. Mi* **11**, 789462 (2022).

23. X. Lei, X. Dong, R. Ma, W. Wang, X. Xiao, Z. Tian, C. Wang, Y. Wang, L. Li, L. Ren, F. Guo, Z. Zhao, Z. Zhou, Z. Xiang, J. Wang, Activation and evasion of type I interferon responses by SARS-CoV-2. *Nat. Commun.* **11**, 3810 (2020).

24. C. Huang, Y. Wang, X. Li, L. Ren, J. Zhao, Y. Hu, L. Zhang, G. Fan, J. Xu, X. Gu, Z. Cheng, T. Yu, J. Xia, Y. Wei, Y. Wu, W. Xie, W. Yin, H. Li, M. Liu, Y. Xiao, H. Gao, L. Guo, J. Xie, G. Wang, R. Jiang, Z. Gao, Q. Jin, J. Wang, B. Cao, Clinical features of patients infected with 2019 novel coronavirus in Wuhan, China. *Lancet* **395**, 497–506 (2020).

25. M. Z. Tay, C. M. Poh, L. Rénia, P. A. MacAry, L. F. P. Ng, The trinity of COVID-19: Immunity, inflammation and intervention. *Nat. Rev. Immunol.* **20**, 363–374 (2020).

26. W. Haussner, A. P. DeRosa, D. Haussner, J. Tran, J. Torres-Lavoro, J. Kamler, K. Shah, COVID-19 associated myocarditis: A systematic review. *Am. J. Emerg. Medicine* **51**, 150–155 (2021).

27. B. F. L. Lai, L. D. Huyer, R. X. Z. Lu, S. Drecun, M. Radisic, B. Zhang, InVADE: Integrated vasculature for assessing dynamic events. *Adv. Funct. Mater.* **27**, 1703524 (2017).

28. B. F. L. Lai, R. X. Z. Lu, L. D. Huyer, S. Kakinoki, J. Yazbeck, E. Y. Wang, Q. Wu, B. Zhang, M. Radisic, A well plate–based multiplexed platform for incorporation of organoids into an organ-on-a-chip system with a perfusable vasculature. *Nat. Protoc.* **16**, 2158–2189 (2021).

29. R. X. Z. Lu, B. F. L. Lai, T. Benge, E. Y. Wang, L. D. Huyer, N. Rafatian, M. Radisic, Heart-on-a-Chip Platform for Assessing Toxicity of Air Pollution Related Nanoparticles. *Adv. Mater. Technologies* **6**, 2000726 (2021).

30. S. Marchiano, T.-Y. Hsiang, A. Khanna, T. Higashi, L. S. Whitmore, J. Bargehr, H. Davaapil, J. Chang, E. Smith, L. P. Ong, M. Colzani, H. Reinecke, X. Yang, L. Pabon, S. Sinha, B. Najafian, N. J. Sniadecki, A. Bertero, M. Gale, C. E. Murry, SARS-CoV-2 infects human pluripotent stem cell-derived cardiomyocytes, impairing electrical and mechanical function. *Stem Cell Rep.* **16**, 478–492 (2021).

31. L. Chen, X. Li, M. Chen, Y. Feng, C. Xiong, The ACE2 expression in human heart indicates new potential mechanism of heart injury among patients infected with SARS-CoV-2. *Cardiovasc. Res.* **116**, cvaa078 (2020).

32. G. Gauchotte, V. Venard, M. Segondy, C. Cadoz, A. Esposito-Fava, D. Barraud, G. Louis, SARS-Cov-2 fulminant myocarditis: An autopsy and histopathological case study. *Int. J. Leg. Med.* **135**, 577–581 (2021).

33. M. C. Pontelli, Í. A. Castro, R. B. Martins, L. L. Serra, F. P. Veras, D. C. Nascimento, C. M. Silva, R. S. Cardoso, R. Rosales, R. Gomes, T. M. Lima, J. P. Souza, B. C. Vitti, D. B. Caetité, M. H. F. de Lima, S. D. Stumpf, C. E. Thompson, L.-M. Bloyet, J. E. Toller-Kawahisa, M. C. Giannini, L. P. Bonjorno, M. I. F. Lopes, S. S. Batah, L. Siyuan, R. Luppino-Assad, S. C. L. Almeida, F. R. Oliveira, M. N. Benatti, L. L. F. Pontes, R. C. Santana, F. C. Vilar, M. Auxiliadora-Martins, P.-Y. Shi, T. M. Cunha, R. T. Calado, J. C. Alves-Filho, D. S. Zamboni, A. T. Fabro, P. Louzada-Junior, R. D. R. Oliveira, S. P. J. Whelan, F. Q. Cunha, E. Arruda, SARS-CoV-2 productively infects primary human immune system cells in vitro and in COVID-19 patients. *J. Mol. Cell Biol.* **14**, mjac021 (2022).

34. B. K. Patterson, E. B. Francisco, R. Yogendra, E. Long, A. Pise, H. Rodrigues, E. Hall, M. Herrera, P. Parikh, J. Guevara-Coto, T. J. Triche, P. Scott, S. Hekmati, D. Maglinte, X. Chang, R. A. Mora-Rodríguez, J. Mora, Persistence of SARS CoV-2 S1 protein in CD16+ monocytes in post-acute sequelae of COVID-19 (PASC) up to 15 months post-infection. *Front. Immunol.* **12**, 746021 (2022).

35. N. Huot, C. Planchais, P. Rosenbaum, V. Contreras, B. Jacquelin, C. Petitdemange, M. Lazzerini, E. Beaumont, A. Orta-Resendiz, F. A. Rey, R. K. Reeves, R. L. Grand, H. Mouquet, M. Müller-Trutwin, SARS-CoV-2 viral persistence in lung alveolar macrophages is controlled by IFN-γ and NK cells. *Nat. Immunol.* **24**, 2068–2079 (2023).

36. D. Scozzi, M. Cano, L. Ma, D. Zhou, J. H. Zhu, J. A. O'Halloran, C. W. Goss, A. M. Rauseo, Z. Liu, S. K. Sahu, V. Peritore, M. Rocco, A. Ricci, R. Amodeo, L. Aimati, M. Ibrahim, R. R. Hachem, D. Kreisel, P. A. Mudd, H. S. Kulkarni, A. E. Gelman, Circulating mitochondrial DNA is an early indicator of severe illness and mortality from COVID-19. *Jci. Insight* **6**, e143299 (2021).

37. M. Blot, M. Jacquier, L.-S. A. Glele, G. Beltramo, M. Nguyen, P. Bonniaud, S. Prin, P. Andreu, B. Bouhemad, J.-B. Bour, C. Binquet, L. Piroth, J.-P.-P. de Barros, D. Masson, J.-P. Quenot, P.-E. Charles; Pneumochondrie study group, F. Aptel, A. Dargent, M. Georges, L. Labruyère, L. Lagrost, A. Large, S. Monier, J.-B. Roudaut, C. Thomas, CXCL10 could drive longer duration of mechanical ventilation during COVID-19 ARDS. *Crit. Care* **24**, 632 (2020).

38. D. B. Zorov, M. Juhaszova, S. J. Sollott, Mitochondrial reactive oxygen species (ROS) and ROS-induced ROS release. *Physiol. Rev.* **94**, 909–950 (2014).

39. Z. Z. Chen, L. Johnson, U. Trahtemberg, A. Baker, S. Huq, J. Dufresne, P. Bowden, M. Miao, J.-A. Ho, C.-C. Hsu, C. C. dos Santos, J. G. Marshall, Mitochondria and cytochrome components released into the plasma of severe COVID-19 and ICU acute respiratory distress syndrome patients. *Clin. Proteomics* **20**, 17 (2023).

40. R. Zhou, A. S. Yazdi, P. Menu, J. Tschopp, A role for mitochondria in NLRP3 inflammasome activation. *Nature* **469**, 221–225 (2011).

41. A. P. West, G. S. Shadel, Mitochondrial DNA in innate immune responses and inflammatory pathology. *Nat. Rev. Immunol.* **17**, 363–375 (2017).

42. N. Khandelwal, J. Simpson, G. Taylor, S. Rafique, A. Whitehouse, J. Hiscox, L. A. Stark, Nucleolar NF-κB/RelA mediates apoptosis by causing cytoplasmic relocalization of nucleophosmin. *Cell Death Differ.* **18**, 1889–1903 (2011).

43. R. J. Mills, S. J. Humphrey, P. R. J. Fortuna, M. Lor, S. R. Foster, G. A. Quaife-Ryan, R. L. Johnston, T. Dumenil, C. Bishop, R. Rudraraju, D. J. Rawle, T. Le, W. Zhao, L. Lee, C. Mackenzie-Kludas, N. R. Mehdiabadi, C. Halliday, D. Gilham, L. Fu, S. J. Nicholls, J. Johansson, M. Sweeney, N. C. W. Wong, E. Kulikowski, K. A. Sokolowski, B. W. C. Tse, L. Devilée, H. K. Voges, L. T. Reynolds, S. Krumeich, E. Mathieson, D. Abu-Bonsrah, K. Karavendzas, B. Griffen, D. Titmarsh, D. A. Elliott, J. McMahon, A. Suhrbier, K. Subbarao, E. R. Porrello, M. J. Smyth, C. R. Engwerda, K. P. A. MacDonald, T. Bald, D. E. James, J. E. Hudson, BET inhibition blocks inflammation-induced cardiac dysfunction and SARS-CoV-2 infection. *Cell* **184**, 2167–2182.e22 (2021).

44. K. Dzobo, H. Chirirwa, C. Dandara, W. Dzobo, Coronavirus disease-2019 treatment strategies targeting interleukin-6 signaling and herbal medicine. *Omics J. Integr. Biology* **25**, 13–22 (2021).

45. P. C. Robinson, D. F. L. Liew, H. L. Tanner, J. R. Grainger, R. A. Dwek, R. B. Reisler, L. Steinman, M. Feldmann, L.-P. Ho, T. Hussell, P. Moss, D. Richards, N. Zitzmann, COVID-19 therapeutics: Challenges and directions for the future. *Proc. Natl Acad. Sci. U.S.A.* **119**, e2119893119 (2022).

46. P. Jirak, V. van Almsick, D. Dimitroulis, M. Mirna, C. Seelmaier, Z. Shomanova, B. Wernly, D. Semo, D. Dankl, M. Mahringer, M. Lichtenauer, U. C. Hoppe, H. Reinecke, R. Pistulli, R. Larbig, L. J. Motloch, Dexamethasone improves cardiovascular outcomes in critically ill COVID-19, a real world scenario multicenter analysis. *Front. Med.* **9**, 808221 (2022).

47. R. C. Group, P. Horby, W. S. Lim, J. R. Emberson, M. Mafham, J. L. Bell, L. Linsell, N. Staplin, C. Brightling, A. Ustianowski, E. Elmahi, B. Prudon, C. Green, T. Felton, D. Chadwick, K. Rege, C. Fegan, L. C. Chappell, S. N. Faust, T. Jaki, K. Jeffery, A. Montgomery, K. Rowan, E. Juszczak, J. K. Baillie, R. Haynes, M. J. Landray, Dexamethasone in hospitalized patients with COVID-19. *New Engl. J. Med.* **384**, 693–704 (2020).

48. S. Gurunathan, M. H. Kang, J.-H. Kim, Diverse effects of exosomes on COVID-19: A perspective of progress from transmission to therapeutic developments. *Front. Immunol.* **12**, 716407 (2021).

49. D. J. Schneider, J. M. Speth, L. R. Penke, S. H. Wettlaufer, J. A. Swanson, M. Peters-Golden, Mechanisms and modulation of microvesicle uptake in a model of alveolar cell communication. *J. Biol. Chem.* **292**, 20897–20910 (2017).

50. E. Urciuoli, B. Peruzzi, Inhibiting extracellular vesicle trafficking as antiviral approach to corona virus disease 2019 infection. *Front. Pharmacol.* **11**, 580505 (2020).

51. A. L. Lightner, V. Sengupta, S. Qian, J. T. Ransom, S. Suzuki, D. J. Park, T. I. Melson, B. P. Williams, J. J. Walsh, M. Awili, Bone marrow mesenchymal stem cell-derived extracellular vesicle infusion for the treatment of respiratory failure from COVID-19. *Chest*, **164**, 1444–1453 (2023).

52. C. Hum, J. Loiselle, N. Ahmed, T. A. Shaw, C. Toudic, J. P. Pezacki, MicroRNA mimics or inhibitors as antiviral therapeutic approaches against COVID-19. *Drugs* **81**, 517–531 (2021).

53. S. Nersisyan, N. Engibaryan, A. Gorbonos, K. Kirdey, A. Makhonin, A. Tonevitsky, Potential role of cellular miRNAs in coronavirus-host interplay. *Peerj.* **8**, e9994 (2020).

54. C. Siniscalchi, A. D. Palo, A. Russo, N. Potenza, Human microRNAs interacting with SARS-CoV-2 RNA sequences: Computational analysis and experimental target validation. *Front. Gen.* **12**, 678994 (2021).

55. C. Xie, Y. Chen, D. Luo, Z. Zhuang, H. Jin, H. Zhou, X. Li, H. Lin, X. Zheng, J. Zhang, P. Wang, J. Zhao, Y. Zhao, H. Huang, Therapeutic potential of C1632 by inhibition of SARS-CoV-2 replication and viral-induced inflammation through upregulating let-7. *Signal Transduct. Target. Ther.* **6**, 84 (2021).

56. X. Lian, J. Zhang, S. M. Azarin, K. Zhu, L. B. Hazeltine, X. Bao, C. Hsiao, T. J. Kamp, S. P. Palecek, Directed cardiomyocyte differentiation from human pluripotent stem cells by modulating Wnt/β-catenin signaling under fully defined conditions. *Nat. Protoc.* **8**, 162–175 (2013).

57. Y. Zhao, N. Rafatian, N. T. Feric, B. J. Cox, R. Aschar-Sobbi, E. Y. Wang, P. Aggarwal, B. Zhang, G. Conant, K. Ronaldson-Bouchard, A. Pahnke, S. Protze, J. H. Lee, L. D. Huyer, D. Jekic, A. Wickeler, H. E. Naguib, G. M. Keller, G. Vunjak-Novakovic, U. Broeckel, P. H. Backx, M. Radisic, A platform for generation of chamber-specific cardiac tissues and disease modeling. *Cell* **176**, 913–927.e18 (2019).

58. Y. Zhao, N. Rafatian, E. Y. Wang, N. T. Feric, B. F. L. Lai, E. J. Knee-Walden, P. H. Backx, M. Radisic, Engineering microenvironment for human cardiac tissue assembly in heart-on-a-chip platform. *Matrix Biol.* **85**, 189–204 (2020).